Monthly Notices of the ROYAL ASTRONOMICAL SOCIETY

MNRAS **434,** 1264–1286 (2013) doi:10.1093/mnras/stt1087
Advance Access publication 2013 July 9

The build-up of nuclear stellar cusps in extreme starburst galaxies and major mergers

S. Haan,[1,2⋆] L. Armus,[2] J. A. Surace,[2] V. Charmandaris,[3,4,5] A. S. Evans,[6,7] T. Diaz-Santos,[2] J. L. Melbourne,[8] J. M. Mazzarella,[9] J. H. Howell,[2] S. Stierwalt,[5] D. C. Kim,[7] T. Vavilkin,[10] D. B. Sanders,[11] A. Petric,[8] E. J. Murphy,[12] R. Braun,[1] C. R. Bridge[8] and H. Inami[13]

[1]*CSIRO Astronomy and Space Science, ATNF, PO Box 76, Epping 1710, Australia*
[2]*Spitzer Science Center, California Institute of Technology, Pasadena, CA 91125, USA*
[3]*IESL/Foundation for Research and Technology – Hellas, GR-71110 Heraklion, Greece*
[4]*Chercheur Associé, Observatoire de Paris, F-75014 Paris, France*
[5]*Department of Physics and Institute of Theoretical and Computational Physics, University of Crete, GR-71003 Heraklion, Greece*
[6]*Department of Astronomy, University of Virginia, PO Box 400325, Charlottesville, VA 22904, USA*
[7]*National Radio Astronomy Observatory, 520 Edgemont Road, Charlottesville, VA 22903, USA*
[8]*Department of Astronomy, California Institute of Technology, Pasadena, CA 91125, USA*
[9]*Infrared Processing & Analysis Center, MS 100-22, California Institute of Technology, Pasadena, CA 91125, USA*
[10]*Department of Physics and Astronomy, SUNY Stony Brook, Stony Brook, NY 11794, USA*
[11]*Institute for Astronomy, University of Hawaii, Honolulu, HI 96822, USA*
[12]*The Observatories, Carnegie Institute of Washington, 813 Santa Barbara Street, Pasadena, CA 91101, USA*
[13]*National Optical Astronomy Observatory, 950 N. Cherry Ave, Tucson, AZ 85719, USA*

Accepted 2013 June 14. Received 2013 June 13; in original form 2013 March 14

ABSTRACT

Nuclear stellar cusps are defined as central excess light component in the stellar light profiles of galaxies and are suggested to be stellar relics of intense compact starbursts in the central ∼100–500 pc region of gas-rich major mergers. Here, we probe the build-up of nuclear cusps during the actual starburst phase for a complete sample of luminous infrared galaxy (LIRG) systems (85 LIRGs, with $11.4 < \log{[L_{\rm IR}/{\rm L}_{\odot}]} < 12.5$) in the Great Observatories All-sky LIRG Survey sample. Cusp properties are derived via 2D fitting of the nuclear stellar light imaged in the near-infrared (NIR) by the *Hubble Space Telescope* and have been combined with mid-infrared (IR) diagnostics for active galactic nucleus (AGN)/starburst characterization. We find that nuclear stellar cusps are resolved in 76 per cent of LIRGs (merger and non-interacting galaxies). The cusp strength and luminosity increase with far-IR luminosity (excluding AGN) and merger stage, confirming theoretical models that starburst activity is associated with the build-up of nuclear stellar cusps. Evidence for ultracompact nuclear starbursts is found in ∼13 per cent of LIRGs, which have a strong unresolved central NIR light component but no significant contribution of an AGN. The nuclear NIR surface density (measured within 1 kpc radius) increases by a factor of ∼5 towards late merger stages. A careful comparison to local early-type galaxies with comparable masses reveals (a) that local (U)LIRGs have a significantly larger cusp fraction and (b) that the majority of the cusp LIRGs have host galaxy luminosities (*H* band) similar to core ellipticals which are roughly one order in magnitude larger than those for cusp ellipticals.

Key words: galaxies: evolution – galaxies: interactions – galaxies: nuclei – galaxies: starburst.

1 INTRODUCTION

While extreme starburst galaxies and major mergers represent only a small fraction of galaxies observed today, observational and theoretical arguments suggest that most massive galaxies must have

⋆E-mail: Sebastian.Haan@csiro.au

evolved through at least one active starburst and merger phase, transforming spirals into massive ellipticals and triggering the most rapid and intense star formation (SF) known in our Universe. The last decades have brought significant progress in understanding the formation of elliptical galaxies with the following picture emerging: during a merger process, tidal torques drive rapid inflows of gas into the centres of galaxies while violent relaxation acts on stars present in gas-rich progenitor discs producing the remnant spheroid (e.g. Barnes & Hernquist 1992). However, the highest phase-space density material can be found in the galactic centres, which comes from gas dissipation in the final, merger-induced central starburst imprinting a central 'extra light' component or stellar 'cusp' into the surface-brightness profiles of merger remnants (e.g. Kormendy & Sanders 1992; Mihos & Hernquist 1994b; Hopkins, Cox & Hernquist 2008c).

In particular, the advent of the *Hubble Space Telescope* (*HST*) has brought sufficient angular resolution to reveal the nuclear light profiles in large samples of early-type galaxies and merger remnants. Evidence for a nuclear cusp build-up has been found in a significant fraction of these early-type galaxies and merger remnants (Lauer et al. 1992; Crane et al. 1993; Ferrarese et al. 1994; Jaffe et al. 1994; Lauer et al. 1995; Faber et al. 1997; Seigar et al. 2002; Graham & Guzmán 2003; Rothberg & Joseph 2004; Côté et al. 2007; Hopkins et al. 2008b; Kormendy et al. 2009). Moreover, these observations suggest that ellipticals can be separated into two different types of nuclear brightness profiles, namely cusp (characterized by a steep inner slope) and core ellipticals (flat profile towards the centre). Follow-up studies have shown a strong dependence on the optical luminosity of the host galaxy, leading to a dichotomy between core and cusp galaxies, with core galaxies dominating at the highest luminosities and cusp galaxies at the lowest (Faber et al. 1997; Quillen, Bower & Stritzinger 2000; Ravindranath et al. 2001; Graham & Guzmán 2003; Rothberg & Joseph 2004; Lauer et al. 2007). The finding that giant elliptical galaxies are slow rotating and low-luminosity elliptical galaxies rapidly rotating (see e.g. Davies & Illingworth 1983; Bender 1988; Cappellari et al. 2007; Emsellem et al. 2007) suggests that the formation of cores and cusps is linked to the dynamics of the merger process or progenitors (for recent review, see Kormendy et al. 2009).

The most popular explanation is that cusp galaxies are produced in dissipative, gas-rich (wet) mergers, while core galaxies are produced in dissipationless, gas-poor (dry) mergers (Faber et al. 1997). Several studies suggest that merger progenitors of core ellipticals may have been even different from all galaxies seen today (e.g. Buitrago et al. 2008; van der Wel et al. 2008; Naab & Ostriker 2009), and are very unlikely cusp ellipticals (Kormendy et al. 2009). Recent observations also indicate that the central stellar light deficit $L_{\rm def}$ in core ellipticals is correlated with the mass of the central stellar black hole (BH; Kormendy & Bender 2009) and that core and cusp galaxies might follow a different $M_{\rm BH}-M_{\rm spheroid}$ relation (Graham 2012). This would suggest a slightly different mechanism linking the formation of the central massive BH with its host galaxy evolution.

However, until recently there has been little observational evidence on the build-up of these cusps during the actual merger-induced starburst stage. While previous ground-based observations (e.g. Wright et al. 1990; James et al. 1999; Rothberg & Joseph 2004) have revealed that a significant fraction of merger remnants seem to exhibit radial profiles similar to elliptical galaxies based on their large-scale appearance (at radii of several kpc), we are now able to link for the first time the stellar light distribution and merger-induced starburst in the central kpc for a large sample of nearby active starburst mergers.

In particular one galaxy population, the luminous infrared galaxies (LIRGs; i.e. $L_{\rm IR} \geq 10^{11}\,{\rm L}_{\odot}$[1]), provides a perfect laboratory to test current theories about the formation of nuclear cusps and elliptical galaxies. Although very rare at low redshift, LIRGs are ∼1000 times more abundant and dominate the total IR energy density emitted at redshifts of $z \sim 1$–2 when SF in our Universe was at its peak and most of the galaxies stellar mass is building up (Elbaz et al. 2002; Le Floc'h et al. 2005; Bridge et al. 2007; Caputi et al. 2007; Magnelli et al. 2009). Multiwavelength imaging surveys of local LIRGs and ultraLIRGs (ULIRGs, $L_{\rm IR} \geq 10^{12}\,{\rm L}_{\odot}$) have shown that with increasing IR luminosity, the star formation rate (SFR), the fraction of sources hosting an active galactic nuclei (AGN) and the fraction of sources with interaction features significantly increase (Armus, Heckman & Miley 1989; Veilleux et al. 1995; Veilleux, Sanders & Kim 1997; Kim & Sanders 1998; Kim, Veilleux & Sanders 1998; Murphy et al. 1999, 2001). Moreover, the projected nuclear separation in sources with double nuclei is significantly smaller for ULIRGs than for LIRGs (Haan et al. 2011a), confirming the picture that most ULIRGs evolve at a later merger stage than LIRGs.

However, due to high column densities of gas and dust, it is almost impossible to reveal the circumnuclear regions and to identify the nuclei in LIRGs at optical wavelengths. High-resolution rest-frame near-infrared (NIR) imaging of their nuclear region with *HST* has revealed that the majority of (U)LIRGs with $L_{\rm IR} \geq 10^{11}\,{\rm L}_{\odot}$ have double nuclei, nearly two times more than those identified in the rest-frame optical light (Haan et al. 2011a). This, without even considering issues such as sensitivity and spatial resolution, implies strong limitations on the ability to detect the true nuclear structure and merger stage of LIRGs at higher redshifts ($z \gtrsim 1.5$), even if observed in the NIR. Although (U)LIRGs at high redshift likely differ in some of their properties from local (U)LIRGs (e.g. in merger fraction, size of starburst, SFR efficiencies, etc.) due to higher gas fractions and smaller galaxy separations at earlier epochs, high-resolution observations of local ULIRGs still provide the best laboratory to study the nature of these galaxies.

Despite recent progress in simulating the formation of nuclear cusps via merging of gas-rich progenitor galaxies (e.g. Hopkins et al. 2009a,b), several important questions are still open. (1) How much stellar mass is typically built up in nuclear cusps and what are the critical time-scales for cusp formation? (2) Is there a link between the strength of cusps in LIRGs and the current rate of SF in these galaxies? (3) Is the fraction of cusps in LIRGs the same as in elliptical galaxies? Do LIRGs display a similar bimodality between the presence of cusps and the stellar mass of the host galaxy and what are the implications for the formation and evolution of elliptical galaxies and spheroids? (4) Are nuclear cusps present only in merger-induced starburst galaxies or can cusps also form in isolated galaxies? If so, what is the mechanism that triggers the gas-dissipation and nuclear starburst in non-interacting galaxies with no apparent interaction features in the NIR and optical light (Haan et al. 2011a; Kim et al. 2013)?

The Great Observatories All-sky LIRG Survey (GOALS; see Armus et al. 2009) provides an excellent sample to address these questions, combining high-resolution multiwavelength *HS*T observations (NICMOS/WFC3 *H* band, ACS *I* and *B* band) with mid-IR (MIR) and far-IR diagnostics (*Spitzer* IRS, IRAC, MIPS, *Herschel*

[1] IR luminosity $L_{\rm IR} = L(8$–$1000\ \mu{\rm m})$ based on IRAS 12, 25, 60 and 100 μm flux densities as defined in Sanders & Mirabel (1996).

PACS, SPIRE) for a complete sample of (U)LIRGs in the local Universe. Moreover, a wealth of additional multiwavelength data is available, ranging from X-ray (*Chandra*), ultraviolet (UV; *GALEX*) to radio (JVLA, ATCA) and submillimetre observations (CARMA, ALMA).

Our previous GOALS *HST* NICMOS study (Haan et al. 2011a) has shown a tremendous increase of the bulge compactness as a function of merger stage, suggesting that cusp formation might play a significant role in these galaxies. Here, we combine our previous *HST* NICMOS *H*-band sample with new WFC3 *H*-band observation for the remaining galaxies of the high-luminosity LIRG sample $L_{\rm IR} \geq 10^{11.4}\,{\rm L}_{\odot}$, and resolve their nuclear cusps using 2D fitting of the 'Nuker' profile (Lauer et al. 1995). This allows us to study the cusp properties in detail over a large range of merger stages and IR luminosities.

The outline of this paper is as follows. In Section 2 we describe the sample, the *HST* observations and the data reduction. The NIR light fitting procedure and the parametrization of cusps are specified in Section 3.1. The derived results are presented in Section 4, including the distribution of cusps, their possible correlation with IR luminosity and AGN activity, the build-up of cusps as a function of the merger stage sequence, as well as possible systematic errors and dependences. In Section 5, we derive estimates of the stellar mass build-up in these cusps and constrain the time-scales required to form them based on their current SFR and evolution as a function of merger stage. Moreover, we carefully compare the (U)LIRG cusp properties to those of local spheroidal galaxies and discuss the implications for formation scenarios of elliptical galaxies as well as possible mechanisms for cusp formation in non-interacting galaxies. The last point of our discussion is the ultracompact nuclear starburst and estimates of their SFR densities in the central 100 pc of (U)LIRGs. A synopsis of the main findings and conclusions is provided in Section 6.

2 SAMPLE AND OBSERVATIONS

The GOALS NIR imaging programme targets the nuclear regions of all systems in the *IRAS* Revised Bright Galaxy Sample (RBGS; Sanders et al. 2003) with $\log{[L_{\rm IR}/{\rm L}_{\odot}]} > 11.4$. The RBGS is a complete sample of all extragalactic objects with $f_{\nu}(60\,\mu{\rm m}) \geq 5.24$ Jy, covering the entire sky surveyed by *IRAS* at Galactic latitudes $|b| > 5^{\circ}$. The RBGS contains 201 LIRGs, of which 88 have luminosities of $\log{[L_{\rm IR}/{\rm L}_{\odot}]} > 11.4$, the luminosity at which the local space density of LIRGs exceeds that of optically selected galaxies. These galaxies are the most luminous members of the GOALS sample and they are predominantly mergers and strongly interacting galaxies (Haan et al. 2011a). Most of the single spiral galaxies or widely separated, weakly/non-interacting pairs in GOALS are filtered out by this luminosity threshold. The redshift range of our sample is $0.01 < z < 0.05$ and hence the galaxies are bright and well resolved due to their large angular size. The final range in far-IR luminosity is $11.4 < \log{[L_{\rm IR}/{\rm L}_{\odot}]} < 12.5$. An overview of our sample is given in Table 1.

Our previous study (Haan et al. 2011a) included only the *HST* NICMOS (camera NIC2) images since NICMOS failed during the execution of this programme, and not all targets in the complete sample of LIRGs were observed. Here, we present new results based on the analysis of the complete *HST* NIR sample, including new *HST* WFC3 images for the rest of our sample. The *HST* WFC3 data have been obtained using the *F160W* filter for 13 LIRGs within a total time of 13 orbits (programme 11235, P.I. Surace) and are combined with the 88 pointings of 73 LIRGs of Haan et al. (2011a) that already have high-quality archival NICMOS data (see Table 1 for an overview of our sample). Note that the LIRG system Arp240 was only partially observed with NICMOS (NGC 5257) and has been completed with WFC3 which observed the other merger component (NGC 5258). The WFC3 data were collected with a field of view (FOV) of 136 arcsec × 123 arcsec and a pixel size of 0.13 arcsec. The data reduction and calibration have been done using the standard *HST* pipeline. Additional corrections were made to the individual frames to adjust for bias offsets and we recombined the images using the STIS software.

A World Coordinate System (WCS) correction has been performed to align with the *HST* ACS images, which were registered using star position references from Two Micron All Sky Survey (2MASS). We carefully applied a WCS transformation to our NICMOS and WFC3 images given the corrected *HST* ACS images using corresponding reference points in both images, such as stars not catalogued, bright star cluster knots or similar unresolved features.

3 DERIVING THE NUCLEAR PROPERTIES USING THE NUKER PROFILE WITH GALFIT

3.1 The NUKER profile

Fitting the light profile of galaxies is far from trivial and the choice of the appropriate profile fit function depends on the structural components, physical scales and the galaxy types of interest. For this study, we have chosen the Nuker profile which was introduced by Lauer et al. (1995) to fit the nuclear profile of nearby galaxies observed with *HST* and is a double power law with the parametric form

$$I(r) = 2^{(\beta-\gamma)/\alpha} I_{\rm b} \left(\frac{r_{\rm b}}{r}\right)^{-\gamma} \left[1 + \left(\frac{r}{r_{\rm b}}\right)^{\alpha}\right]^{(\gamma-\beta)/\alpha} \quad (1)$$

where β is the outer power-law slope, γ is the inner slope, $r_{\rm b}$ is the 'break radius' between the outer and inner profile, and α moderates the sharpness of the transition (more rapid transition with larger α).

Although the Nuker profile is very well suited to describe the central region of galaxies, it does not link the outer profile with a physical representation of large-scale galaxy features (such as bars, bulge and disc). However, the typical radii of cusps are 100–1000 pc (on average 250 pc), which is well within the limits of the Nuker profile. While single and double Sérsic profiles have been applied to measure the cusp in ellipticals in some studies as well (e.g. Graham & Guzmán 2003; Hopkins et al. 2009a), a combination of Sérsic profiles would lead to degeneracies in fitting more complicated structures such as a combination of disc, bulge and cusp which is more typical in LIRGs. We have tested a combination of multiple Sérsic profiles, but found that fitting simultaneously all structural components of a galaxy would reveal reasonable results only in very few LIRGS without complicated structure. The argument against a full decomposition of the entire galaxy's structure is that every component fit is strongly dependent on the outcome of the other components, which would (a) make the interpretation of the multiple Sérsic profiles difficult and (b) would not allow a coherent measurement of the cusp over the large morphological variety of LIRGs. The main advantage of the Nuker profile is that it is not an extrapolation of the outer galaxy profile and does not depend on the large-scale structure of a galaxy unlike a single or combination of multiple Sérsic profiles.

Table 1. Sample overview.

Name	RA (J2000)	Dec. (J2000)	$\log[L_{IR}/L_{\odot}]$	D (Mpc)	*HST* ID	Instrument
NGC 0034	00:11:06.61	−12:06:27.4	11.49	84.1	7268	NICMOS
ARP 256N	00:18:50.12	−10:21:42.6	11.48	117.5	11235	NICMOS
ARP 256S	00:18:50.90	−10:22:37.0	11.48	117.5	11235	NICMOS
MCG +12-02-001	00:54:04.20	+73:05:06.0	11.5	69.8	10169	NICMOS
IC 1623E	01:07:46.49	−17:30:22.5	11.71	85.5	7219	NICMOS
IC 1623W	01:07:47.42	−17:30:25.9	11.71	85.5	7219	NICMOS
MCG -03-04-014	01:10:08.90	−16:51:10.0	11.65	144	11235	NICMOS
CGCG 436-030	01:20:02.70	+14:21:43.0	11.69	134	11235	NICMOS
IRAS 01364-1042	01:38:52.90	−10:27:11.0	11.85	198	11235	NICMOS
III ZW 035	01:44:30.52	+17:06:07.9	11.64	119	11235	NICMOS
NGC 0695	01:51:14.20	+22:34:57.0	11.68	139	11235	NICMOS
MRK 1034W	02:23:18.91	+32:11:19.2	11.64	145	11235	NICMOS
MRK 1034E	02:23:22.00	+32:11:50.0	11.64	145	11235	NICMOS
UGC 02369S	02:54:01.77	+14:58:14.2	11.67	136	11235	NICMOS
UGC 02369N	02:54:01.81	+14:58:35.6	11.67	136	11235	NICMOS
IRASF 03359+1523	03:38:46.95	+15:32:54.5	11.55	152	11235	NICMOS
ESO 550-IG025N	04:21:19.87	−18:48:36.9	11.51	138.5	11235	NICMOS
ESO 550-IG025S	04:21:20.06	−18:48:56.3	11.51	138.5	11235	NICMOS
NGC 1614	04:33:59.91	−08:34:44.3	11.65	67.8	9726	NICMOS
ESO 203-IG001	04:46:49.42	−48:33:31.1	11.86	235	11235	NICMOS
VII Zw 031	05:16:46.60	+79:40:13.0	11.99	240	9726	NICMOS
IRAS 05223+1908	05:25:16.30	+19:10:45.0	11.65	128	11235	WFC3
IRAS 06076−2139	06:09:45.81	−21:40:23.7	11.65	165	11235	WFC3
ESO 255-IG007N	06:27:22.04	−47:10:42.0	11.9	173	11235	NICMOS
ESO 255-IG007S	06:27:23.12	−47:11:03.1	11.9	173	11235	NICMOS
AM 0702−601N	07:03:24.10	−60:15:23.0	11.64	141	11235	NICMOS
AM 0702-601S	07:03:28.63	−60:16:42.9	11.64	141	11235	NICMOS
2MASX J07273754−0254540	07:27:37.55	−02:54:54.1	12.39	400	11235	WFC3
2MASX J08370182−4954302	08:37:01.80	−49:54:30.0	11.62	210	11235	NICMOS
NGC 2623	08:38:24.00	+25:45:17.0	11.6	84.1	7219	NICMOS
ESO 060-IG016	08:52:30.77	−69:01:59.8	11.82	210	11235	NICMOS
IRAS-F08572+3915	09:00:25.40	+39:03:54.0	12.16	264	9726	NICMOS
IRAS 09111−1007	09:13:37.61	−10:19:24.8	12.06	246	11235	WFC3
UGC 04881	09:15:55.1	+44:19:55.00	11.74	178	11235	WFC3
UGC 05101	09:35:51.40	+61:21:11.0	12.01	177	9726	NICMOS
IRAS-F10173+0828	10:19:59.9	+08:13:34.00	11.86	224	11235	WFC3
NGC 3256	10:27:51.03	−43:54:18.2	11.64	38.9	9735	NICMOS
IRAS-F10565+2448	10:59:18.20	+24:32:37.0	12.08	197	7219	NICMOS
Arp 148	11:03:53.20	+40:50:57.0	11.62	158	11235	WFC3
IRAS-F11231+1456	11:25:45.00	+14:40:36.0	11.64	157	9726	NICMOS
IC 2810	11:25:49.52	+14:40:06.9	11.64	157	11235	WFC3
NGC 3690W	11:28:30.91	+58:33:45.2	11.93	50.7	9726	NICMOS
NGC 3690E	11:28:33.50	+58:33:45.2	11.93	50.7	9726	NICMOS
IRAS-F12112+0305	12:13:45.90	+02:48:39.0	12.36	340	7219	NICMOS
WKK 0787	12:14:22.10	−56:32:33.0	11.65	114.5	11235	NICMOS
VV 283	13:01:50.8	+04:20:0.00	11.68	175	11235	WFC3
ESO 507-G070	13:02:52.30	−23:55:18.0	11.56	106	11235	WFC3
NGC 5010	13:12:26.30	−15:47:52.00	11.50	45	11235	WFC3
WKK 2031	13:15:06.30	−55:09:23.0	12.32	144	11235	NICMOS
UGC 08335W	13:15:31.15	+62:07:44.4	11.81	142	11235	NICMOS
UGC 08335E	13:15:35.29	+62:07:27.5	11.81	142	11235	NICMOS
UGC 08387	13:20:35.30	+34:08:22.0	11.73	110	7219	NICMOS
NGC 5256	13:38:17.79	+48:16:35.1	11.56	129	7328	NICMOS
NGC 5257	13:39:52.97	+00:50:22.5	11.56	129	11235	NICMOS
NGC 5258	13:39:57.68	+00:49:49.80	11.56	129	11235	WFC3
UGC 08696	13:44:41.90	+55:53:12.1	12.21	173	9726	NICMOS
NGC 5331S	13:52:16.17	+02:06:01.2	11.66	155	11235	NICMOS
NGC 5331N	13:52:16.54	+02:06:28.8	11.66	155	11235	NICMOS
IRAS-F14348-1447	14:37:38.20	−15:00:24.0	12.39	387	7219	NICMOS
IRAS-F14378-3651	14:40:58.91	−37:04:31.8	12.23	315	7896	NICMOS
UGC 09618S	14:57:00.34	+24:36:24.7	11.74	157	11235	NICMOS
UGC 09618N	14:57:00.70	+24:37:01.5	11.74	157	11235	NICMOS
VV 705	15:18:06.30	+42:44:37.0	11.92	183	11235	WFC3

Table 1 – *continued*

Name	RA (J2000)	Dec. (J2000)	$\log[L_{\rm IR}/L_\odot]$	D (Mpc)	*HST* ID	Instrument
ESO 099-G004	15:24:58.20	−63:07:34.0	11.74	137	11235	NICMOS
IRAS-F15250+3608	15:26:59.30	+35:58:37.0	12.08	254	7219	NICMOS
UGC 09913	15:34:57.20	+23:30:10.9	12.28	87.9	9726	NICMOS
NGC 6090	16:11:40.60	+52:27:25.0	11.58	137	7219	NICMOS
2MASX J16191179−0754026	16:19:11.80	−07:54:03.0	11.62	128	11235	NICMOS
ESO 069-IG006N	16:38:11.84	−68:26:10.4	11.98	212	11235	NICMOS
ESO 069-IG006S	16:38:13.48	−68:27:19.3	11.98	212	11235	NICMOS
IRAS 16399−0937	16:42:40.20	−09:43:14.0	11.63	114	11235	NICMOS
NGC 6240	16:52:58.70	+02:24:04.0	11.93	116	7219	NICMOS
IRASF 17132+5313	17:14:20.24	+53:10:30.8	11.96	232	11235	NICMOS
IRAS-F17138−1017	17:16:35.60	−10:20:38.0	11.49	84	10169	NICMOS
IRAS-F17207−0014	17:23:22.20	−00:17:02.0	12.46	198	7219	NICMOS
IRAS 18090+0130	18:11:38.42	+01:31:38.8	11.65	134	11235	NICMOS
IC 4689	18:13:40.28	−57:44:53.5	11.62	81.9	11235	NICMOS
IRAS 18293−3413	18:32:41.22	−34:11:26.7	11.88	86	11235	NICMOS
NGC 6670W	18:33:33.77	+59:53:15.6	11.65	129.5	11235	NICMOS
NGC 6670E	18:33:37.70	+59:53:23.0	11.65	129.5	11235	NICMOS
NGC 6786S	19:10:53.90	+73:24:37.0	11.49	113	11235	NICMOS
UGC 11415	19:10:53.90	+73:24:37.7	11.49	113	11235	NICMOS
NGC 6786N	19:11:04.44	+73:25:37.4	11.49	113	11235	NICMOS
ESO 593-IG008	19:14:30.98	−21:19:06.8	11.93	222	11235	NICMOS
IRAS-F19297−0406	19:32:22.28	−04:00:01.1	12.45	395	7896	NICMOS
IRAS 19542+1110	19:56:35.39	+11:19:03.0	12.12	295	11235	NICMOS
IRAS 20351+2521	20:37:17.80	+25:31:38.0	11.61	151	11235	NICMOS
II ZW 096	20:57:23.94	+17:07:39.5	11.94	161	11235	NICMOS
ESO 286-IG019	20:58:26.80	−42:39:00.0	12.06	193	11235	NICMOS
IRAS 21101+5810	21:11:29.82	+58:23:07.2	11.81	174	11235	NICMOS
ESO 239-IG002	22:49:39.90	−48:50:58.0	11.84	191	11235	NICMOS
IRAS-F22491−1808	22:51:49.30	−17:52:24.0	12.2	351	7219	NICMOS
NGC 7469 / IC5283	23:03:17.88	+08:53:39.3	11.65	70.8	11235	NICMOS
ESO 148-IG002	23:15:46.79	−59:03:13.0	12.06	199	7896	NICMOS
IC 5298	23:16:00.71	+25:33:24.0	11.6	119	11235	NICMOS
ESO 077-IG014	23:21:04.44	−69:12:54.8	11.76	186	11235	NICMOS
NGC 7674	23:27:56.70	+08:46:45.0	11.56	125	11235	NICMOS
IRASF 23365+3604	23:39:01.30	+36:21:09.8	12.2	287	11235	NICMOS
IRAS 23436+5257	23:46:05.59	+53:14:01.0	11.57	149	11235	NICMOS
UGC 12812W / MRK0331	23:51:18.73	+20:34:42.9	11.5	79.3	11235	NICMOS
UGC 12812E / MRK0331	23:51:26.80	+20:35:10.0	11.5	79.3	11235	NICMOS

Notes. Overview of the properties of our 85 LIRG systems (101 pointings). Columns (1): source name from NED, (2): right ascension (J2000), (3): source declination (J2000), (4): The luminosity distance in Mpc (adopted from Armus et al. 2009), (5): The total IR luminosity in $\log_{10}$ solar units, (6): the data origin given by the ID of the observational programme, (7): the *HST* instrument used to obtain the 1.6 μm data fit in this paper.

3.2 GALFIT fitting and cusp parameter estimates

To derive detailed information about the structural properties of LIRGS we performed a 2D decomposition of all galaxies in our sample using GALFIT (Peng et al. 2010). In this paper, we focus on an accurate measurement of the central light component, in particular the nuclear slope as parametrized by the Nuker profile to obtain the cusp and core properties of LIRGs. This approach focuses on an accurate parametrization of the very centre (<1 kpc), in particular the stellar cusp, which appears at much smaller scales than those of our previous *HST* NICMOS study (Haan et al. 2011a) where we used multiple Sérsic component fits (Sérsic 1968) to decompose the galaxy primarily into bulge and disc component (this is not possible with a Nuker profile). The surface-brightness profile which is fitted in equation (1) is defined as

$$\mu_{\rm b} = -2.5\,\log_{10}\left(\frac{I_{\rm b}}{t_{\rm exp}\Delta x\,\Delta y}\right) + {\rm mag}zpt, \qquad (2)$$

where the image exposure time $t_{\rm exp}$ is in seconds, the pixel scale Δx and Δy in arcsec, and magzpt is the magnitude zero-point. In all there are a total of nine parameters to fit ($x_{\rm centre}$, $y_{\rm centre}$, μ, $r_{\rm b}$, α, β, γ, and the inclination and position angle of the galaxy).

Nearly 15 per cent of the galaxies in our sample are not suitable for fitting their nuclear profiles which is caused by several circumstances: highly disturbed centre, dust obscuration in edge on galaxies and dominant strong point sources. We performed a careful analysis of each galaxy and identified the cases where a nuclear fit would not work or might lead to large uncertainties. However, most of these galaxies are selected out due to their geometrical alignment (edge on) and hence do not introduce a physical selection bias. This results in a representative sample of 81 galaxies for which we have obtained nuclear NUKER profiles.

Running GALFIT on an image requires some initial preparation. The desired fitting region and sky background must be provided, and the *HST* instrumental point spread function (PSF) image, bad pixel mask (if needed) and pixel noise map must be generated. The integrated galaxy counts per second are converted to an apparent Vega magnitude (see more details in Haan et al. 2011a), the required *HST* PSF image is simulated with the TINYTIM code (Krist & Hook 1997) using a pixel scale identical to that of the observations, and the uncertainty images are generated by the *HST* reduction pipeline and used as weighting images required for GALFIT to perform the χ^2 minimization. The PSF image is utilized to fit the unresolved component in the centres of these galaxies, which can originate either from a central AGN or nuclear SF.

After these preparation steps we carried out an iterative fitting process since GALFIT requires initial guesses for each component it fits and uses a Levenberg–Marquardt downhill-gradient algorithm to determine the minimum χ^2 based on the input guesses. At first we fitted Nuker profiles that are centred on the galaxies' nuclei (typically 1to 2 nuclei per image). For merger systems that have two or more galaxies, we take advantage of GALFIT's ability to fit simultaneously multiple components at different spatial regions. Initial parameter guesses for the centre, position angle, inclination and sky background have been estimated with Sérsic profiles (Haan et al. 2011a), but have been kept free for the new model fit. A PSF fit has been tested for all sources but only applied in the final fit for those where a GALFIT solution was found. The centre coordinates were fixed when it was necessary (e.g. in cases where PSF and Nuker profile centres drift too far away due to starburst region or other components that might mimic a point source). In several cases, we have tested a range of fitting regions to obtain the best fit of the transition between outer and inner profiles. The outer radius used for the fitting is typically 1–3 kpc, which is roughly 3–10 times the cusp radius, which is defined here as the break radius of the Nuker law. One important point to be cautioned about when using the Nuker profile is to ensure that the transition parameter α is large enough to separate inner and outer profile because, for example, a low α value ($\alpha < 2$) can be reproduced by simultaneously having a high γ and a low β, which is a serious possibility for degeneracy (see Peng et al. 2010). Therefore, in cases where α behaved unreasonably, either $\alpha < 2$ or $\alpha > 10$, we tested several values in the range of $2 < \gamma < 10$, and fixed α at the value for which the best solution was found. Fitted models were selected only as long as the model parameters were all well behaved, i.e. requiring that all parameters such as break radius, inner/outer slope values and transition parameter converged within the range of reasonable values. The best fit was chosen based on the χ^2 for each model and the quality of the residual image. Since this study focuses only on the nuclear parametrization we have not attempted to find a perfect solution for the entire galaxy, for which the Nuker profile fitting is likely not suited in any case. All in all we have tried to find the most robust fit for the nuclear slope that can be applied in a homogeneous way among all sources in our sample using one main component (plus a PSF component) rather than splitting the model, e.g. in three or more Sérsic profiles (cusp, bulge, disc, bar, etc.) which introduces many more free parameters and possible interpretations.

3.3 Example of a strong cusp galaxy: the nuclear NIR properties of NGC 1614

Cusps manifest themselves as strong central excess light on top of the normal light profile of a galaxy (i.e. stellar bulge, disc and often a bar). A typical example of a strong cusp galaxy is NGC 1614 whose *HST* and GALFIT residual images are presented in Fig. 1 and the radial light profile in Fig. 2. This galaxy exhibits a cusp with a slope of $\gamma = 1.36$ and a break radius of ∼0.34 arcsec (110 pc) where the transition between the outer disc and the additional cusp component occurs. The size of the cusp is similar to the spatial size of Paα emission (see Section 4.6) which is a strong indicator of ongoing SF on the cusp scale. This demonstrates that the stellar cusp is linked to the current SF in this galaxy. The residual image reveals a nuclear spiral structure and a large number of circumnuclear cluster, but typically at less than one magnitude lower surface brightness than the cusp. An image of the cusp component together with several other examples can be found in Appendix B.

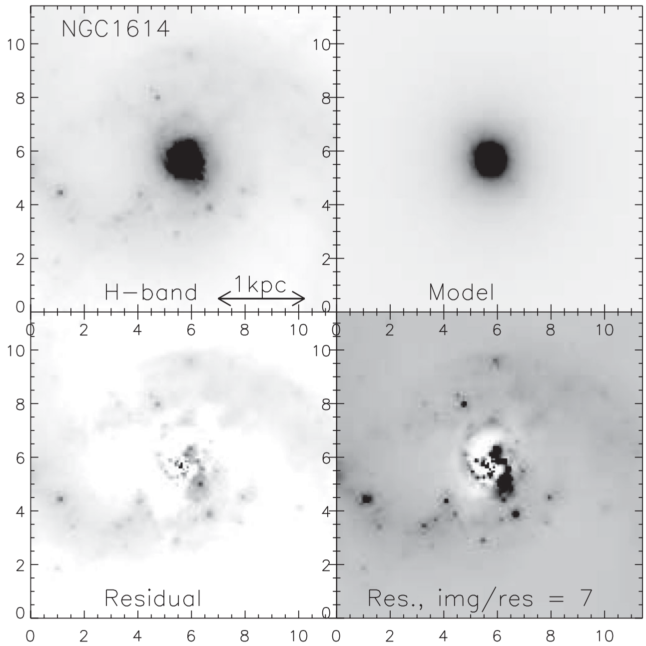

Figure 1. GALFIT output images for NGC 1614 (scaled with the square root of intensity). Top left: region of NICMOS image that is fitted. Top right: Galfit model. Bottom left: residual image (shows the difference between model and NICMOS image) with the same brightness level as the NICMOS image. Bottom right: residual image scaled to its maximum brightness (the brightness ratio of NICMOS image to scaled residual map is shown as well at the bottom) to highlight the faint diffuse emission, spiral structure and clusters remaining in the model-subtracted data. The axes are in units of arcsec and the figures are oriented in the observational frame.

4 SURVEY RESULTS

4.1 Cusp-to-core ratio and cusp luminosities

The NIR luminosity[2] of the cusp $L_{\rm cusp}$ is computed by subtracting the integrated magnitude with γ set to zero (equal to the extrapolated outer profile for the centre) from the total integrated magnitude $M_{\rm Nuker}$ within the cusp radius $r_{\rm b}$,

$$M_{\rm cusp} = \int_0^{r_{\rm b}} M_{\rm Nuker} - \int_0^{r_{\rm b}} M_{\rm Nuker,\gamma=0}. \quad (3)$$

Except for γ, all parameter values are the same between both integrated magnitudes. Therefore, the cusp luminosity is defined as the residual light of the fitted Nuker profile after subtraction of the reference profile which is here the inward extrapolation of the outer power-law fit of the Nuker profile. This calculation of the cusp luminosity is more robust and accurate than just fitting the light

[2] All luminosities derived from our *HST* NIR images (i.e. $L_{\rm cusp}$, $L_{\rm PSF}$, $L_{\rm nuc}$ and $L_{\rm Nuker}$) refer to the H-band solar luminosity.

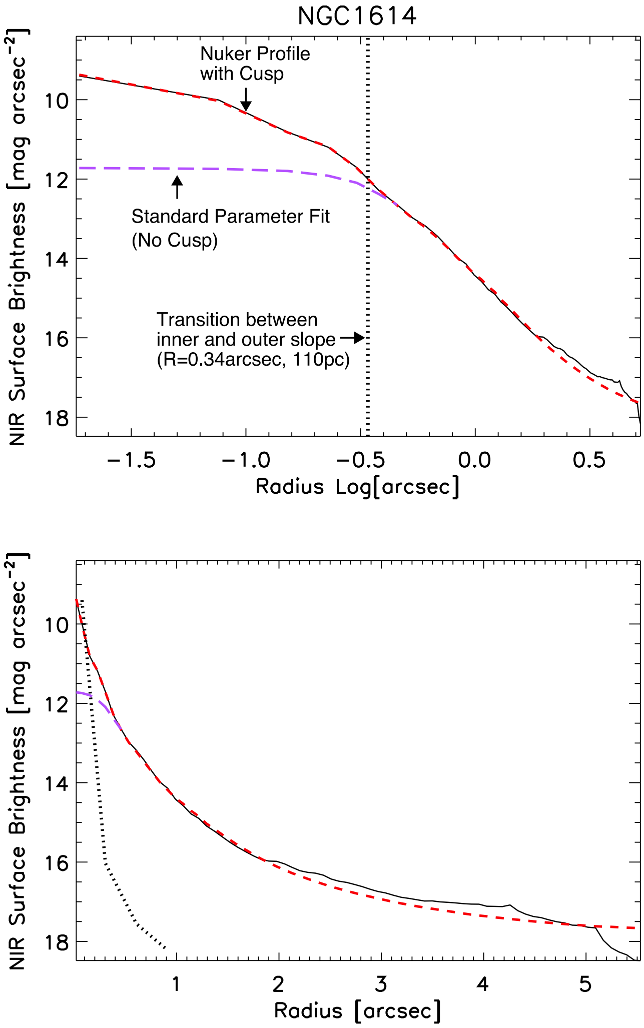

Figure 2. The radial profile of NGC 1614 as an example for a strong cusp slope. Top (logarithmic radial scale): the solid black line is the actual data as observed with *HST* NICMOS at 1.6 μm. The long dashed line shows a fit of the outer envelope with no cusp component, while the short dashed line (as well as the data) shows an additional inner power-law component as fitted with GALFIT in 2D (Peng et al. 2010) with a slope of $\gamma = 1.36$. The transition between the outer disc and the additional cusp component occurs at a radius of ∼0.34 arcsec (110 pc). Bottom (linear radial scale): the dotted line indicates the spatial resolution (NICMOS PSF) which is scaled to the maximum of the measured Nuker profile.

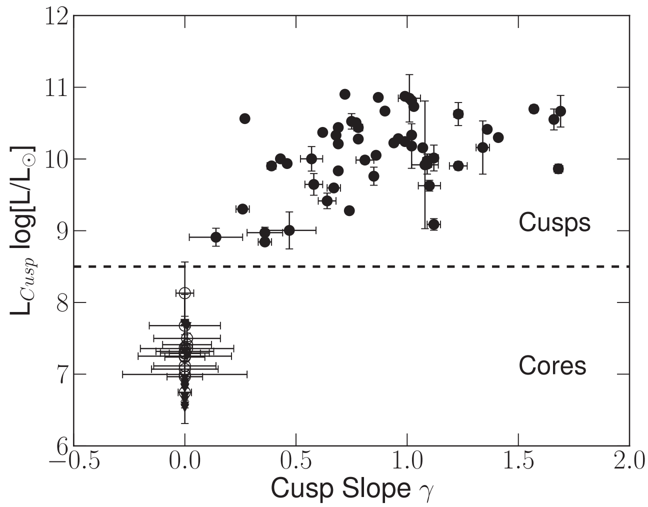

Figure 3. The NIR (1.6 μm) cusp luminosity $L_{\rm cusp}$ as a function of the cusp slope γ. Upper luminosity limits for sources with $\gamma \sim 0$ have been derived based on the uncertainty in γ (typically d$\gamma \sim \pm 0.1$).

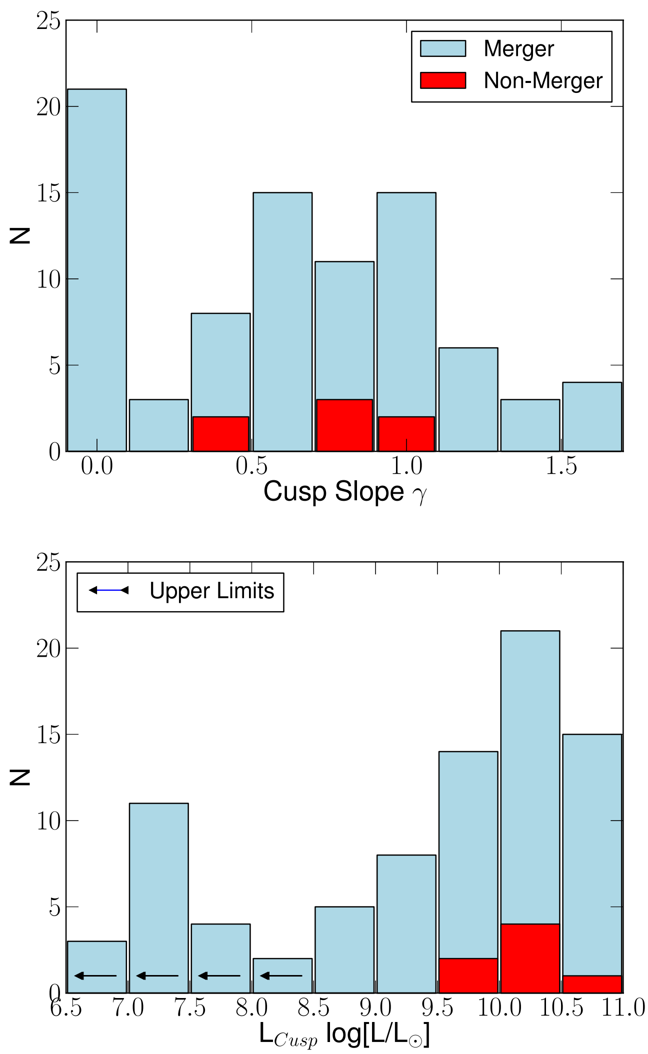

Figure 4. Top: histogram of the cusp slope (γ) of our sample of interacting (blue) and non-interacting LIRGs (red), indicating a dichotomy between core ($\gamma \sim 0$) and cusp galaxies ($\gamma > 0.3$). Bottom: histogram of the cusp luminosity with upper limits for core galaxies (left arrows).

rising above a fitted outer envelope (e.g. using a Sérsic profile), which is complicated in our galaxies by the mix of multiple outer components (bulge, bar, disc) as discussed in Section 3.1. Note that the luminosity of the unresolved component $L_{\rm PSF}$ is separated from this computation. Upper limits for core galaxies ($\gamma \sim 0$) have been derived based on the uncertainty in γ (typically d$\gamma \sim \pm 0.1$), but this does not take into account the spatial resolution limit and the possibility of an unresolved cusp (see Section 4.7).

Fig. 3 shows the relation between cusp slope and cusp luminosity for 77 galaxies with good fit models. Only those models are accepted for which all parameters such as break radius, inner/outer slope values and transition parameter converged within the range of reasonable values (see Section 3.2). The cusp luminosity increases as a function of cusp slope in the interval of $0 < \gamma < 1$, and no significant increase is found for $\gamma > 1$. Fig. 4 shows the distribution of the slope (γ) in our sample ranging from $\gamma = 0$ to $\gamma = 1.7$. The histogram reveals one peak at $\gamma \sim 0 \pm 0.1$ (core galaxies) and the other (broader) peak at $\gamma \sim 0.8 \pm 0.4$. We use the distribution in $\gamma = 0$ to define core ($\gamma < 0.3$) and cusp galaxies ($0.3 > \gamma$), as referred hereafter, with a cusp/core ratio 3.2:1. Out of our sample of 77 galaxies with good profile fits, 59 (76 per cent) have nuclear cusps. The naming conventions vary in the literature, in general cusp galaxies are defined to have steep power-law surface-brightness profiles in the centre, while core galaxies have surface-brightness profiles with a flat central core. All derived cusp properties are listed in Table 2. We find no correlation between the total NIR luminosity of the host galaxy and the NIR cusp luminosity or cusp slope.

The cusp luminosity distribution follows the two peaks as seen in the γ distribution. Based on the optical and NIR morphology (tidal tails, merger components) we have classified our LIRG sample into major merger and non-major merger (no major companion, tidal tails or strong disturbance, see Haan et al. 2011a). Our results are shown in Fig. 4. While there are only seven apparent non-mergers in our *HST F160W* sample, they all have cusp luminosities above $\log{[L_{\rm cusp}/{\rm L}_{\odot}]} = 9.5$, with an average luminosity of $\log{[L_{\rm cusp}/{\rm L}_{\odot}]} = 10.3 \pm 0.3$. The merging LIRGs on the other hand, have a much larger range in cusp luminosities, and 24 per cent have only upper limits with cusp luminosities below

Table 2. Nuclear properties and merger classification.

Name	$RA_{\rm Cusp}$ (J2000)	$Dec._{\rm Cusp}$ (J2000)	MS	$L_{\rm IR}$ log10[$L_{\odot}$]	γ	$R_{\rm cusp}$ (arcsec)	$L_{\rm cusp}$ log10[$L_{\odot}$]	$L_{\rm nuc}$ log10[$L_{\odot}$]	$L_{\rm PSF}$ log10($L_{\odot}$)	SB
NGC 0034	00:11:06.545	−12:06:27.24	5	11.43	1.02 ± 0.01	0.38 ± 0.05	10.33 ± 0.01	11.0 ± 0.01	9.52 ± 0.02	cen
ARP 256N	00:18:50.130	−10:21:41.69	3	10.45	0.4 ± 0.27	0.11 ± 0.12	7.52 ± 1.19	10.4 ± 0.04	8.07 ± 0.06	off
ARP 256S	00:18:50.872	−10:22:36.56	3	11.44	0.0 ± 0.11	0.12 ± 0.06	≤7.3	10.66 ± 0.04	9.34 ± 0.03	cen
MCG +12-02-001	00:54:04.005	+73:05:05.40	3	11.5	1.68 ± 0.02	0.26 ± 0.06	9.86 ± 0.06	11.0 ± 0.01	9.32 ± 0.04	cen
IC 1623E	01:07:46.553	−17:30:22.61	3	11.71	0.64 ± 0.02	1.55 ± 0.37	9.57 ± 0.21	10.06 ± 0.2	≤6.6	off
MCG -03-04-014	01:10:08.916	−16:51:09.58	0	11.65	0.46 ± 0.01	0.77 ± 0.06	9.94 ± 0.01	10.97 ± 0.01	9.71 ± 0.02	cen
CGCG 436-030	01:20:02.622	+14:21:42.35	2	11.69	0.01 ± 0.21	0.13 ± 0.06	≤7.36	10.56 ± 0.05	10.29 ± 0.01	cen
IRAS 01364−1042	01:38:52.855	−10:27:11.41	5	11.85	0.01 ± 0.11	0.12 ± 0.06	≤7.41	10.48 ± 0.03	≤7.33	cen
III ZW 035 n1	01:44:30.554	+17:06:09.18	3	11.64	0.0 ± 0.02	0.21 ± 0.05	≤7.37	10.61 ± 0.01	≤6.89	cen
III ZW 035 n2	01:44:30.537	+17:06:08.84	3	11.64	0.51 ± 0.01	0.24 ± 0.05	9.17 ± 0.01	10.41 ± 0.01	≤6.89	off
NGC 0695	01:51:14.334	+22:34:56.01	0	11.68	0.78 ± 0.01	1.42 ± 0.09	10.28 ± 0.03	10.75 ± 0.01	9.37 ± 0.03	cen
MRK 1034W	02:23:18.956	+32:11:18.73	2	11.16	0.85 ± 0.01	0.4 ± 0.1	9.76 ± 0.13	10.86 ± 0.04	9.4 ± 0.04	cen
MRK 1034E	02:23:21.950	+32:11:48.83	2	11.47	0.0 ± 0.04	0.3 ± 0.06	≤8.13	11.13 ± 0.02	≤7.06	cen
ESO 550-IG02N	04:21:19.976	−18:48:39.31	2	11.27	0.0 ± 0.09	0.1 ± 0.06	≤7.24	10.66 ± 0.03	≤7.02	cen
ESO 550-IG02S	04:21:20.018	−18:48:57.14	2	11.13	0.0 ± 0.07	0.1 ± 0.05	≤7.29	10.85 ± 0.02	≤7.02	cen
NGC 1614	04:34:00.015	−08:34:45.11	5	11.66	1.36 ± 0.01	0.33 ± 0.05	10.41 ± 0.01	10.94 ± 0.01	≤6.4	cen
ESO 203-IG001	04:46:49.534	−48:33:29.90	3	11.86	0.69 ± 0.01	0.62 ± 0.06	9.83 ± 0.02	10.51 ± 0.01	8.79 ± 0.08	cen
VII Zw 031	05:16:46.482	+79:40:12.84	0	11.99	0.81 ± 0.02	0.49 ± 0.08	10.28 ± 0.17	11.00 ± 0.07	9.61 ± 0.06	cen
ESO 255-IG007S	06:27:21.754	−47:10:35.74	3	11.78	0.14 ± 0.12	0.22 ± 0.07	8.91 ± 0.13	10.97 ± 0.05	≤7.21	cen
AM 0702-601N	07:03:24.258	−60:15:22.49	1	11.46	–	–	–	–	11.28 ± 0.01	cen
AM 0702-601S	07:03:28.626	−60:16:44.66	1	11.19	0.42 ± 0.12	0.31 ± 0.12	9.21 ± 0.5	10.53 ± 0.25	≤7.03	cen
IRAS 08355−4944	08:37:01.881	−49:54:30.58	3	11.62	–	–	–	–	10.47 ± 0.03	cen
NGC 2623	08:38:24.099	+25:45:16.70	5	11.6	≥0.0	≤0.08	≥6.96	10.63 ± 0.02	9.58 ± 0.01	cen
IRAS-F 08572+3915	09:00:25.361	+39:03:55.31	3	12.16	1.12 ± 0.02	0.81 ± 0.19	10.01 ± 0.18	10.28 ± 0.12	9.69 ± 0.02	cen
IRAS 09111−1007E	09:13:38.837	−10:19:19.72	1	11.39	0.01 ± 0.1	1.63 ± 0.11	≤8.5	9.98 ± 0.05	≤7.52	cen
IRAS 09111−1007W	09:13:36.449	−10:19:29.95	1	11.95	–	–	–	10.97 ± 0.02	9.78 ± 0.05	cen
UGC 4881N	09:15:55.518	+44:19:58.04	2	11.58	0.0 ± 0.13	0.21 ± 0.07	≤7.32	10.65 ± 0.03	≤7.24	cen
UGC 4881S	09:15:54.685	+44:19:51.46	2	11.24	0.58 ± 0.04	0.58 ± 0.13	9.65 ± 0.15	10.61 ± 0.06	9.24 ± 0.09	cen
UGC 05101	09:35:51.631	+61:21:11.85	5	12.02	1.02 ± 0.01	0.74 ± 0.06	10.81 ± 0.01	11.29 ± 0.01	10.2 ± 0.01	cen
IRAS-F 10173+0828	10:20:00.207	+08:13:33.78	0	11.86	0.94 ± 0.01	0.78 ± 0.06	10.22 ± 0.01	10.65 ± 0.01	9.12 ± 0.06	cen
NGC 3256	10:27:51.254	−43:54:14.00	5	11.64	1.08 ± 0.06	0.64 ± 0.48	9.92 ± 0.89	11.16 ± 0.28	9.78 ± 0.08	cen
IRAS-F 10565+2448	10:59:18.146	+24:32:34.57	2	12.08	0.9 ± 0.01	0.82 ± 0.06	10.67 ± 0.01	11.13 ± 0.01	10.23 ± 0.01	cen
IRAS-F11231+1456	11:25:45.073	+14:40:35.96	1	11.46	0.64 ± 0.04	0.17 ± 0.07	9.42 ± 0.11	10.9 ± 0.05	≤7.13	cen
NGC 3690E	11:28:33.688	+58:33:46.36	3	11.58	0.74 ± 0.01	0.58 ± 0.07	9.28 ± 0.03	10.41 ± 0.02	≤6.15	cen
IRAS-F 12112+0305S	12:13:45.903	+02:48:39.28	4	12.1	1.68 ± 0.01	0.61 ± 0.20	10.56 ± 0.35	10.67 ± 0.28	≤7.8	cen
IRAS-F12112+0305N	12:13:46.022	+02:48:41.67	4	12.05	0.72 ± 0.05	0.31 ± 0.25	9.58 ± 1.06	10.44 ± 0.27	8.75 ± 0.17	cen
WKK 0787	12:14:22.097	−56:32:33.28	0	11.65	1.02 ± 0.01	0.92 ± 0.33	10.18 ± 0.31	10.8 ± 0.14	≤6.85	cen
VV 283	13:01:50.294	+04:20:00.51	5	11.68	0.0 ± 0.16	0.25 ± 0.07	≤7.68	10.83 ± 0.04	9.88 ± 0.04	cen
ESO 507	13:02:52.378	−23:55:17.54	6	11.56	0.0 ± 0.15	0.25 ± 0.08	≤7.07	10.69 ± 0.04	≤6.79	cen
WKK 2031	13:15:06.338	−55:09:22.71	5	12.32	0.99 ± 0.01	0.99 ± 0.06	10.87 ± 0.02	11.3 ± 0.01	9.89 ± 0.1	cen
UGC 08335W	13:15:30.800	+62:07:45.26	2	11.5	1.09 ± 0.02	0.55 ± 0.12	9.93 ± 0.14	10.67 ± 0.06	≤7.04	cen
UGC 08335E	13:15:35.028	+62:07:28.84	2	11.5	0.99 ± 0.01	0.45 ± 0.07	10.24 ± 0.04	10.96 ± 0.02	≤7.04	cen
NGC 5256S	13:38:17.272	+48:16:32.10	3	11.36	0.43 ± 0.01	0.89 ± 0.07	10.0 ± 0.01	10.98 ± 0.01	8.84 ± 0.06	cen
NGC 5256N	13:38:17.762	+48:16:41.17	3	11.13	0.86 ± 0.01	0.88 ± 0.1	10.05 ± 0.04	10.7 ± 0.03	9.28 ± 0.02	cen
NGC 5257	13:39:52.933	+00:50:24.51	2	11.31	1.12 ± 0.04	0.18 ± 0.06	9.47 ± 0.06	10.59 ± 0.02	≤6.96	off
NGC 5258	13:39:57.681	+00:49:50.89	2	11.32	0.49 ± 0.04	0.38 ± 0.06	8.85 ± 0.17	10.5 ± 0.05	≤6.81	off
NGC 5331S	13:52:16.202	+02:06:05.20	3	11.54	0.0 ± 0.28	0.19 ± 0.14	≤7.0	10.84 ± 0.06	≤7.12	cen
NGC 5331N	13:52:16.425	+02:06:31.15	3	11.02	1.1 ± 0.05	0.12 ± 0.06	9.63 ± 0.08	10.88 ± 0.02	≤7.12	cen
IRAS-F 14348−1447N	14:37:38.401	−15:00:21.13	4	12.1	0.0 ± 0.09	0.1 ± 0.06	≤7.62	10.75 ± 0.03	9.92 ± 0.02	cen

Table 2 – *continued*

Name	RA_{Cusp} (J2000)	$ec._{Cusp}$ (J2000)	MS	L_{IR} log10[$L_\odot$]	γ	R_{cusp} (arcsec)	L_{cusp} log10[$L_\odot$]	L_{nuc} log10[$L_\odot$]	L_{PSF} log10[$L_\odot$]	SB
IRAS-F 14348−1447S	14:37:38.288	−15:00:24.14	4	12.1	0.97 ± 0.01	0.38 ± 0.08	10.03 ± 0.07	10.52 ± 0.04	≤7.91	cen
IRAS-F 14378−3651	14:40:59.010	−37:04:31.92	6	12.23	0.96 ± 0.01	0.17 ± 0.05	10.28 ± 0.03	10.99 ± 0.02	9.56 ± 0.05	cen
UGC 09618S	14:57:00.325	+24:36:24.00	1	11.0	1.12 ± 0.03	0.19 ± 0.06	9.09 ± 0.08	10.46 ± 0.01	≤7.13	cen
VV 705N	15:18:06.138	+42:44:45.29	4	11.85	1.23 ± 0.02	1.96 ± 0.35	10.63 ± 0.16	10.69 ± 0.1	9.88 ± 0.11	cen
VV 705S	15:18:06.349	+42:44:38.34	4	11.12	0.87 ± 0.13	0.22 ± 0.1	–	–	−7.26 ± 0.01	cen
ESO 099−G004N	15:24:57.941	−63:07:29.68	3	11.74	1.34 ± 0.03	0.46 ± 0.2	10.16 ± 0.37	10.64 ± 0.25	≤7.01	cen
IRAS F15250+3608	15:26:59.425	+35:58:37.22	5	12.08	–	–	–	10.73 ± 0.16	9.71 ± 0.02	cen
NGC 6090	16:11:40.914	+52:27:27.21	4	11.58	0.2 ± 0.04	0.12 ± 0.01	8.08 ± 0.03	10.67 ± 0.01	≤7.01	cen
ESO 069−IG006N	16:38:11.870	−68:26:08.19	2	11.97	0.08 ± 0.02	1.45 ± 0.03	9.89 ± 0.02	11.02 ± 0.01	≤7.39	cen
ESO 069−IG006S	16:38:13.469	−68:27:16.83	2	10.48	0.57 ± 0.05	0.77 ± 0.17	10.0 ± 0.17	10.66 ± 0.1	≤7.39	cen
IRAS 16399−0937S	16:42:40.177	−09:43:18.77	3	11.0	0.67 ± 0.04	0.3 ± 0.08	9.21 ± 0.12	10.54 ± 0.05	8.83 ± 0.1	off
IRAS 16399−0937N	16:42:40.141	−09:43:13.18	3	11.62	0.36 ± 0.03	0.24 ± 0.06	8.84 ± 0.03	10.41 ± 0.02	≤6.85	cen
NGC 6240S	16:52:58.884	+02:24:03.28	4	11.63	1.01 ± 0.05	0.53 ± 0.2	10.85 ± 0.33	11.44 ± 0.24	≤6.87	cen
NGC 6240N	16:52:58.933	+02:24:04.92	4	11.63	0.54 ± 0.73	0.08 ± 0.16	8.92 ± 6.05	11.02 ± 0.49	≤6.87	cen
IRASF 17132+5313N	17:14:20.449	+53:10:31.96	2	11.65	0.72 ± 0.01	2.05 ± 0.07	10.9 ± 0.01	10.96 ± 0.01	≤7.47	cen
IRASF 17132+5313S	17:14:19.800	+53:10:28.86	2	11.65	0.36 ± 0.08	0.08 ± 0.05	8.97 ± 0.08	10.61 ± 0.03	≤7.47	cen
IRAS-F 17138−1017	17:16:35.791	−10:20:38.81	6	11.49	0.5 ± 0.01	3.0 ± 0.16	10.21 ± 0.03	10.74 ± 0.01	≤6.58	off
IRAS-F 17207−0014	17:23:21.951	−00:17:00.74	5	12.46	0.69 ± 0.01	1.24 ± 0.11	10.44 ± 0.05	10.86 ± 0.02	≤7.33	cen
IRAS 18090+0130	18:11:38.415	+01:31:40.01	2	11.52	0.47 ± 0.12	0.14 ± 0.08	9.0 ± 0.26	10.9 ± 0.08	≤6.99	cen
IC 4689	18:13:40.387	−57:44:54.12	2	10.88	1.07 ± 0.01	1.48 ± 0.09	10.16 ± 0.03	10.72 ± 0.01	9.24 ± 0.03	cen
IRAS 18293−3413	18:32:41.135	−34:11:27.54	1	11.88	1.03 ± 0.01	2.01 ± 0.13	10.73 ± 0.04	11.13 ± 0.02	≤6.61	cen
NGC 6786S	19:10:53.836	+73:24:36.70	2	11.23	0.69 ± 0.01	2.08 ± 0.12	10.21 ± 0.03	10.64 ± 0.02	9.09 ± 0.1	cen
NGC 6786N	19:11:04.295	+73:25:33.40	2	11.15	1.41 ± 0.01	0.65 ± 0.06	10.3 ± 0.02	10.92 ± 0.01	≤7.10	cen
IRAS 19542+1110	19:56:35.785	+11:19:05.09	0	12.12	0.78 ± 0.02	0.18 ± 0.05	10.44 ± 0.02	11.24 ± 0.01	≤7.68	cen
ESO 286-IG019	20:58:26.798	−42:39:00.21	5	12.06	0.81 ± 0.04	0.45 ± 0.06	9.99 ± 0.05	10.76 ± 0.02	9.0 ± 0.29	cen
IRAS 21101+5810	21:11:29.296	+58:23:08.02	2	11.81	0.26 ± 0.03	0.67 ± 0.08	9.3 ± 0.04	10.39 ± 0.04	9.01 ± 0.1	cen
ESO 239-IG002	22:49:39.889	−48:50:58.14	5	11.84	1.57 ± 0.01	0.66 ± 0.09	10.7 ± 0.05	10.94 ± 0.04	10.31 ± 0.02	cen
ESO 148-IG002	23:15:46.744	−59:03:15.74	4	12.06	1.66 ± 0.01	0.52 ± 0.13	10.55 ± 0.15	10.79 ± 0.11	≤7.33	cen
IC 5298	23:16:00.679	+25:33:24.03	0	11.6	0.39 ± 0.02	0.92 ± 0.08	9.9 ± 0.03	10.86 ± 0.02	9.5 ± 0.07	cen
ESO 077-IG014	23:21:05.354	−69:12:47.18	2	11.56	0.0 ± 0.21	0.11 ± 0.07	≤7.25 0.43	11.01 ± 0.06	≤7.28	cen
NGC 7674	23:27:56.715	+08:46:44.41	2	11.54	1.23 ± 0.04	0.19 ± 0.06	9.9 ± 0.06	10.78 ± 0.02	10.53 ± 0.01	cen
IRAS-F 23365+3604	23:39:01.270	+36:21:08.56	5	12.2	1.09 ± 0.02	0.15 ± 0.06	9.98 ± 0.1	10.8 ± 0.05	9.76 ± 0.02	cen
IRAS 23436+5257N	23:46:05.496	+53:14:01.42	4	11.4	0.0 ± 0.14	0.12 ± 0.06	≤7.12	10.67 ± 0.03	9.58 ± 0.01	cen
IRAS 23436+5257S	23:46:05.704	+53:13:56.71	4	11.1	0.01 ± 0.15	0.16 ± 0.06	≤7.5	10.4 ± 0.03	8.82 ± 0.18	cen
UGC 12812W	23:51:18.673	+20:34:41.58	4	9.32	0.0 ± 0.03	0.88 ± 0.27	≤6.75	10.05 ± 0.01	7.1 ± 0.12	cen
UGC 12812E	23:51:26.738	+20:35:10.39	1	11.5	0.68 ± 0.01	1.67 ± 0.06	10.33 ± 0.01	10.94 ± 0.01	≤6.53	cen

Notes. Columns (1): source name from NED, (2): right ascension (J2000) in degree, (3): declination (J2000) in degree, (4): the merger stage classification, (5): the L_{IR} luminosity computed for each merger component (see the text in Section 4.2), (6): the central slope of the Nuker profile γ, (7): the effective break radius (cusp/core radius) between central and outer power law of Nuker profile in arcsec, (8): the cusp luminosity or the upper limit based on the error in γ, (9): the nuclear NIR luminosity integrated over the central area with a radius of 1 kpc, (10): the NIR luminosity of the central unresolved component (*HST* PSF), (11): the identification whether the starburst peak (based on MIPS24 μm emission) is in the centre of the galaxy or offset.

$\log[L_{cusp}/L_\odot] = 8.5$. We discuss the possible reasons for the difference in these distributions in Section 5.4.

4.2 Relationship between current star formation and cusp strength

To test if the central starburst activity in LIRGs is related to the build-up of cusps, we have plotted the measured cusp properties as a function of far-IR luminosity as shown in Fig. 5. The total IR luminosity L_{IR} is a very good tracer of the SFR in LIRGs with SF rates of several tens to hundreds of $M_\odot$ yr^{-1}. However, this is only applicable if most of the L_{IR} originates from starbursts rather than AGN. Therefore, we have selected for this comparison only galaxies that have no dominant AGN contribution to the L_{IR} (polycyclic aromatic hydrocarbon equivalent width, PAH EQW > 0.27; see Petric et al. 2011). A second criterion for this comparison is that the starburst must originate from the centre of the galaxies as indicated by the peak of the *Spitzer* MIPS 24 μm emission (which is the case for 90 per cent of galaxies in our sample). The exclusion of LIRGs with non-nuclear MIR emission is essential since the exact cause of the enhanced emission in these galaxies is not clear (see e.g. Mirabel et al. 1998; Charmandaris, Stacey & Gull 2002; Charmandaris, Le Floc'h & Mirabel 2004; Inami et al. 2010; Haan et al. 2011a; Le Floc'h et al. 2012) and is likely not directly associated with the cusp build-up.

Since most of our LIRGs are merger systems we calculated the individual L_{IR} luminosities for each merger component as described in the following (see also Díaz-Santos et al. 2013). First, we performed an aperture photometry on the MIPS 24 μm images as a proxy of L_{IR} based on the projected distances between the sources. We obtained the total flux of individual galaxies by using a large aperture for isolated sources, and for those in groups, an aperture radius of slightly less than half the distance between the closest sources. These derived fluxes agree within 5 per cent with values previously measured by Howell et al. (2010). For the overlapping galaxies we included in their luminosity uncertainties a factor that

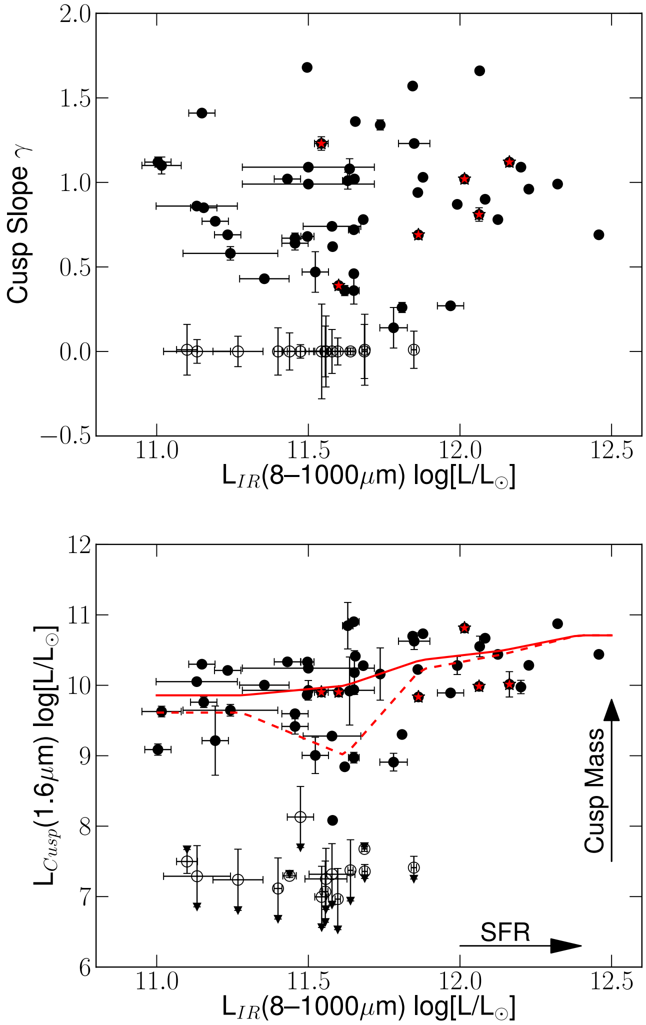

Figure 5. The cusp slope (γ, top) and the cusp luminosity (bottom) as a function of IR luminosity. For core galaxies (arrow down marker) the upper luminosities limits are plotted (based on their uncertainty in γ which is typically ± 0.1). The red solid (dashed) line shows the interpolated mean (median) cusp luminosity $L_{\rm cusp}$ as a function of IR luminosity. Note that galaxies with dominant AGN contribution to the $L_{\rm IR}$ (EQW PAH 6.2 μm < 0.27, diamond marker) have been excluded in the mean values.

accounts for the small apertures used to obtain their photometry and the relative luminosity between the sources. In some cases the sum of the flux of all individual components does not add up to the total flux measured by Howell et al. (2010) for the integrated systems, but the difference is typically not larger than 10 per cent. Hence, we scaled up the individual luminosities proportionally to match up the integrated system luminosity. For merger systems with very small nuclear separation distances and both nuclei covered roughly equally within the 24 μm emission, we have assigned each nuclei half of the $L_{\rm IR}$ luminosity and updated the uncertainties accordingly. The individual $L_{\rm IR}$ luminosities estimated this way and their uncertainties are listed in Table 2.

Fig. 5 shows the cusp NIR luminosity $L_{\rm cusp}$ as a function of $L_{\rm IR}$ for each galaxy. While there is a large scatter at low IR luminosities, the average $L_{\rm cusp}$ is significantly larger at higher $L_{\rm IR}$ luminosities. We note that a similar behaviour is also found if we use the $L_{\rm IR}$ luminosities of the combined merger system. The increase in cusp luminosity can be attributed to the increase in the slope γ and the bulge radius. However, independent of the cusp parameters, we also find that the central NIR surface luminosity within 1 kpc radius increases as a function of $L_{\rm IR}$. Its average value in systems with $\log\,[L_{\rm IR}/{\rm L}_\odot] > 11.9$ is 2.5 times higher compared to the corresponding lower luminosity average. Note again that the unresolved component is not included here. The scatter at low IR luminosities is in agreement with the fact that these galaxies are typically a mix of mergers and non-mergers, which means they might have already gone through a phase of cusp formation or, alternatively, the cusp formation process is intrinsically different between merger-induced and non-merger induced starbursts. In contrast, high IR luminous LIRGs ($\log\,[L_{\rm IR}/{\rm L}_\odot] > 11.9$) are predominantly major mergers. Note that galaxies with dominant AGN contribution to the $L_{\rm IR}$ have been excluded in the statistical analysis but are marked in Fig. 5 for completeness. Our results show that in particular above $\log\,[L_{\rm IR}/{\rm L}_\odot] = 11.9$, all sources have strong cusps ($L_{\rm cusp} \gtrsim 10^{10}$ ${\rm L}_\odot$). The average cusp luminosity increases about a factor of 5 from $\log\,[L_{\rm IR}/{\rm L}_\odot] = [11.0–11.5]$ (mean $L_{\rm cusp}/{\rm L}_\odot = [0.9 \pm 0.9] \times 10^{10}$, median $L_{\rm cusp}/{\rm L}_\odot = 0.52 \times 10^{10}$) to $\log\,[L_{\rm IR}/{\rm L}_\odot] = [12.0–12.5]$ (mean $L_{\rm cusp}/{\rm L}_\odot = [3.8 \pm 1.9] \times 10^{10}$, median $L_{\rm cusp}/{\rm L}_\odot = 3.3 \times 10^{10}$). This corresponds, on average, to an increase in the NIR cusp luminosity of $\sim 3 \times 10^{10}$ ${\rm L}_\odot$. The statistical significance is tested via the Kolmogorov–Smirnov (KS) test which confirms that the distribution of the cusp luminosity between low and high IR luminous LIRGs is not the same (at a probability level of more than 99 per cent). In Section 5.1 we will estimate the associated build-up of stellar mass in these cusps and discuss the implications for SFRs and time-scales.

4.3 Comparison between nuclear stellar structure and mid-IR spectral diagnostics

To study whether the central starburst and cusp growth in LIRGs is accompanied by an AGN activity, we compare our AGN characterization based on MIR diagnostics with the unresolved central component (PSF) in the *HST* NIR images. The MIR AGN characterization is based on the EQW of the 6.2 μm PAH feature, with lower values indicating an excess of hot dust emission which is usually associated with AGN activity (see e.g. Genzel et al. 1998; Sturm et al. 2000; Armus et al. 2007; Desai et al. 2007). Petric et al. (2011) estimated that AGN are responsible for ∼12 per cent of the total bolometric luminosity of local LIRGs based on several MIR line diagnostics measured with the Infrared Spectrograph on *Spitzer*. Lee et al. (2012) have found that half of the (U)LIRGs optically classified as non-Seyferts show AGN signatures in their NIR spectra and that the contribution of buried AGNs to the IR luminosity is 5–10 per cent, which is based on AKARI NIR spectroscopy and MIR spectral energy distribution (SED) fitting for 36 (U)LIRGs. The fraction of AGN-dominated sources stays roughly constant as the merger progresses, while the fraction of composite sources (i.e. those with a weak AGN that does not dominate the emission in the MIR) increases (Stierwalt et al. 2013).

In principle, the presence of a strong unresolved component in the *HST* NIR images (<150 pc, corresponding to the mean *HST* resolution for our sample) indicates a possible central AGN. However, such a PSF can potentially also originate from a very compact starburst (Scoville et al. 2000). In Fig. 6 we investigate if the PAH EQW (measured by Stierwalt et al. 2013) is correlated with the PSF component of the *HST* NIR images. For composite and starburst-dominated sources (PAH EQW > 0.27 μm) the fraction of PSF and non-PSF sources is roughly the same with no apparent increase of PSF luminosity as a function of decreasing PAH EQW. Note that

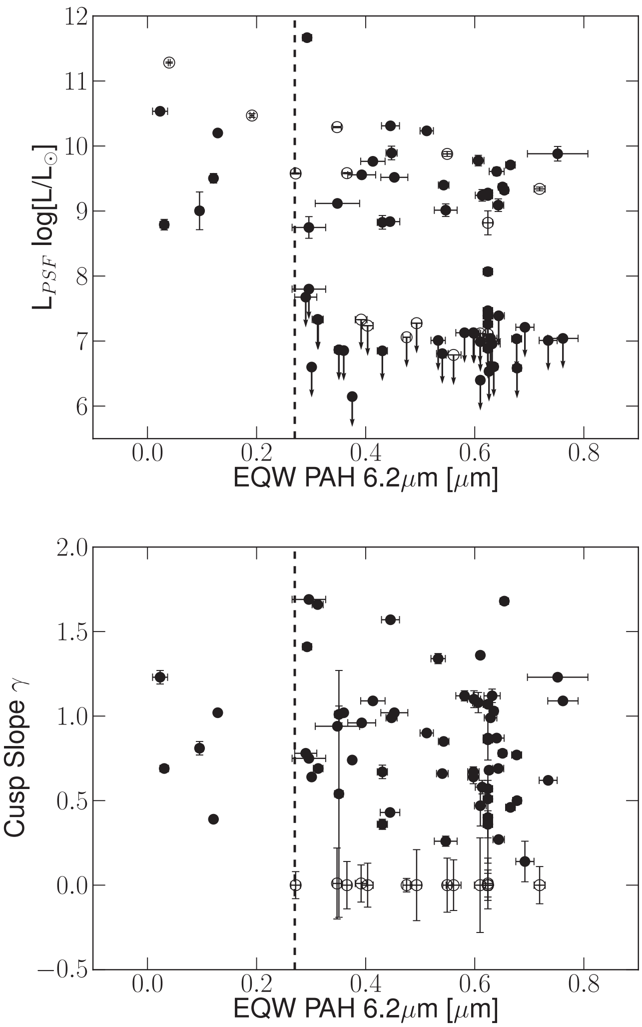

Figure 6. Top: the fitted central unresolved component (*HST* 1.6 μm PSF) as a function of the 6.2 μm PAH EQW. Small EQW indicate a dominant AGN contribution to the IR luminosity (dashed line, EQW $\lesssim$0.27 μm) while the centre of galaxies with larger EQWs are a mix of starburst and AGN light (dashed line, 0.27 μm < EQW < 0.54 μm) or dominated by starbursts (EQW > 0.54 μm). The arrows at the bottom indicate that these are upper limits (uncertainty) of the PSF luminosity for galaxies with no significant PSF measured by GALFIT. Bottom: the cusp slope as a function of the 6.2 μm PAH EQW.

the characterization as AGN (EQW < 0.27), composite (0.27 μm < EQW < 0.54 μm) and starburst (EQW > 0.54 μm) IR-dominated sources has been defined by Petric et al. (2011), but is not meant as a stringent classification. There is a small increase of sources from starburst dominated (EQW > 0.54 μm) to composite sources (0.27 < EQW < 0.54 μm) with the fraction of PSF sources increasing from 40 to 50 per cent, respectively. However, this change is small in comparison to the AGN-dominated IR sources (PAH EQW < 0.27 μm), with all of them exhibiting a strong unresolved central component in the NIR (see Fig. 6), which confirms the presence of a strong AGN in the centre of these sources (ESO 203-IG001, AM 0702-601north, 2MASX J08370182-4954302, UGC 05101, ESO 286-IG019, IC 5298, NGC 7674). However, the PSF luminosity is roughly the same for AGN dominated, composite and starburst sources, which implies that the presence of an AGN does not significantly affect the properties of the *H*-band PSF.

One interesting question is whether there is any relationship between the strength of the cusp and the presence of an AGN. The bottom panel of Fig. 6 shows the cusp slope γ as a function of the EQW of the 6.2μm PAH feature emission. While we find no trend between EQW and cusp strength (in terms of γ and $L_{\rm cusp}$) for starburst and composite sources (EQW > 0.27 μm), all of the sources with a dominant AGN in the MIR (EQW < 0.27 μm and unresolved central NIR component) have cusps (γ > 0.3 and log [$L_{\rm cusp}$/L$_\odot$] > 9.6) rather than cores (γ < 0.3).

4.4 The nuclear unresolved NIR light component: evidence for ultracompact nuclear starbursts?

A significant fraction of our LIRG sample (∼13 per cent) has a substantial unresolved component (*HST* PSF measured with GALFIT) but no detected AGN contribution to the MIR (based on MIR diagnostics with PAH EQW > 0.6, see Section 4.3 and Fig. 6). Interestingly, all of them are LIRGs (log [11.4 < $L_{\rm IR}$/L$_\odot$] < 12) rather than ULIRGs ([$L_{\rm IR}$/L$_\odot$] > 12). Although there are seven ULIRGS with an unresolved component, all of them have PAH EQW < 0.52 and hence we cannot rule out the possibility of an AGN contribution. The mean distance of LIRGs with unresolved component and PAH EQW > 0.6 is 133 Mpc which is even slightly smaller than for the entire sample (mean distance: 153 Mpc), hence a possible distance dependency can be likely ruled out. All of these sources (10) have an unresolved NIR component (log [$L_{\rm PSF}$/L$_\odot$] > 8.5) with a mean luminosity of log [$L_{\rm PSF}$/L$_\odot$] = 9.4. This population of LIRGs spans a large range in far-IR luminosity (mean log [$L_{\rm IR}$/L$_\odot$] = 11.44), merger stages (from non-interacting to late-stage merger), a large range in the nuclear slope γ (including core and cusp galaxies) and a large range in distance. The most likely explanation is that the unresolved nuclear component originates from a very compact starburst that has either build-up a high stellar central density (assuming that most of the NIR light originates from old and intermediate aged stars) and/or is currently active (if most of the NIR light is due to radiation from young stars).

To estimate the stellar density in these galaxies, we have derived their NIR luminosity surface densities $\Sigma_{\rm NIR\text{-}centre}$, which is given by $(L_{\rm PSF} + L_{\rm Nuker})/(\pi R^2_{\rm PSF})$, where $R_{\rm PSF}$ is the spatial limit of the PSF component of *HST* NICMOS and WFC3 (∼0.15 arcsec) converted in kpc, $L_{\rm PSF}$ is the NIR PSF luminosity and $L_{\rm Nuker}$ the integrated light of the Nuker profile within the central aperture (0.15 arcsec). The mean stellar surface density of our compact starburst sample is (2.4 ± 1.2) × 10^5 M$_\odot$ pc^{-2} (within a mean nuclear radius of $\lesssim$100 pc) if we assume a standard mass-to-light ratio in the *H* band $\Upsilon_H = 0.3 \pm 0.15$. The applied Υ_H and its uncertainty is derived from STARBURST99 simulations (Leitherer et al. 1999) using Geneva High and Padova asymptotic giant branch (AGB) tracks, Kroupa initial mass function (IMF), and instantaneous SF with a mass of 10^6 M$_\odot$ and solar metallicity. The lower limit of $\Upsilon_H = 0.15$ is derived from the assumption that the NIR is dominated by young stars (4 Myr) while the upper limit of $\Upsilon_H = 0.45$ is a mix of young, intermediate (50 Myr) and old stellar populations (few 100 Myr) contributing equally to the NIR light. We note that a constant Υ_H for the inner 1 kpc does not take into account local variations due to not direct stellar photospheric emission (i.e. UV light from massive stars that has been extinguished by dust). The derived stellar surface density is similar to the maximum stellar surface density $\Sigma_{\rm max}$ found in a large range of dense stellar systems, including globular clusters, massive star clusters in nearby starbursts, nuclear star clusters in dwarf spheroidals and late-type discs, ultracompact dwarfs, and galaxy spheroids spanning the range from low-mass bulges and ellipticals to massive 'core' ellipticals (Hopkins et al. 2010). NGC 3256 is the nearest LIRG (39 Mpc) of those 10 compact starburst subsample, and subsequently has the largest measured stellar surface density with $\sim 1 \times 10^6$ M$_\odot$ pc^{-2} (within the nuclear radius of 28pc). If we assume an average SFR of $\sim$220 M$_\odot$ yr^{-1} for our galaxies, which is based on the SFR–$L_{\rm IR}$ luminosity relation (Kennicutt 1998), and that at least 10 per cent of the total SF originates from the compact starburst, we estimate a maximal time-scale of 100 Myr to build up the stellar unresolved component in these compact starbursts.

4.5 Nuclear properties along the merger stage sequence

Most of the LIRGs in our sample are major mergers. However, seven LIRGs are isolated undisturbed galaxies, suggesting that mechanisms other than strong gravitational interactions may trigger the IR luminosity in those isolated LIRGs (e.g. minor mergers, high gas fraction and stellar mass, cold gas accretion or other internal dynamical processes). Therefore, these two subclasses of LIRGs, major mergers versus isolated galaxies, are treated separately in our studies. The non-merger/merger separation as well as the merger classification scheme is based on the optical and NIR light distribution (see Table 2 for merger classification). While the *HST* NICMOS/WFC3 *H*-band images reveal the unobscured nuclei and stellar components, the *HST* ACS *I*- and *B*-band images provide a larger FOV for the detection of companion galaxies and are very sensitive for tracing tidal tails and other interaction features which are essential to identify the merger stage. This provides a distinct advantage over using a simple projected nuclear separation to infer the merger stage, which suffers from degeneracies when exploring a large range in stages. To establish a merger classification we carefully separated at first our sample into galaxies that exhibit interaction features (e.g. tidal tails, bridges) or have nearby companions, and those without any interaction features or nearby companions (undisturbed single galaxies), excluding the latter from our merger sequence analysis. The mergers are classified into six different stages (Surace 1998; Surace et al. 1998; Haan et al. 2011a; Kim et al. 2013): 1 – separate galaxies, but discs symmetric (intact) and no tidal tails, 2 – progenitor galaxies distinguishable with discs asymmetric or amorphous and/or tidal tails, 3 – two nuclei in common envelope, 4 – double nuclei plus tidal tails, 5 – single or obscured nucleus with long prominent tails and 6 – single or obscured nucleus with disturbed central morphology and short faint tails. In summary, these stages may be broadly characterized into pre-merger (1), ongoing merger (2, 3, 4) and post-merger LIRGs (5, 6).

Table 3 represents the fraction of cusp galaxies ($\gamma > 0.3$) as a function of merger stage. One puzzling result is the difference in the abundance of cusps between merger and non-merger LIRGs as already indicated in Section 4.1. In detail, all of the non-merger (MS 0) and 86 per cent of separated galaxy pairs that show no interaction signatures (MS 1) have a cusp, which is larger than the average fraction of cusp galaxies in interacting galaxies $\sim$70 per cent). There might be several reasons for this difference and we will discuss several possibilities in more detail in Section 5.2, but note that this comparison may be statistically biased due to the small number of non-interacting LIRGs in our sample.

Table 3. Cusp fraction versus merger stage.

Merger stage	MS 0	MS 1	MS 2	MS 3	MS 4	MS 5
Number of galaxies	7	7	23	17	11	15
Number of cusps	7	6	15	12	8	11
Cusp fraction (per cent)	100	86	65	71	73	73

In Fig. 7, we show a number of nuclear properties as a function of merger stage (excluding MS 0). The cusp slope γ, the cusp luminosity $L_{\rm cusp}$, the cusp surface density $L_{\rm cusp}/(\pi R_{\rm cusp}^2)$ and the total nuclear luminosity $L_{\rm nuc}$ within 1 kpc radius. Most of these properties show evidence for an increase towards the final merger stage (MS 5). A small deviation is found for MS 1, which is probably due to the fact that this merger stage (galaxy pairs that show no interaction features) is likely a mix of merger and non-merger induced starbursts, as already discussed previously. The median value of the cusp slope γ increases by a factor of 1.5 from MS 2 to MS 4/5, and almost a factor of 2 if core galaxies ($\gamma < 0.3$) are taken into account. The statistical significance is tested via the KS test which confirms that the distribution of γ between pre-/mid-merger and late-stage merger bin are not the same (at a probability level of 92 per cent). Also the cusp luminosity $L_{\rm cusp}$ shows a peak at MS 4/5 with an increase of a factor of 3 (from log [$L_{\rm cusp}$/L$_\odot$] = 10.0 at MS 2 to log [$L_{\rm cusp}$/L$_\odot$] $\sim$ 10.5 at MS 4/5) with a KS probability level of >99 per cent. The cusp surface density is significantly larger at the late merger stage (MS 5) of about a factor of 5–10 in comparison to earlier merger stages (MS 1–4) with a KS probability level of 99 per cent. This trend in cusp surface density is confirmed by the increase in the total nuclear luminosity measured within 1 kpc radius towards the late merger stage (increase of a factor of 4–5, KS probability level of 99 per cent). This measurement does not depend

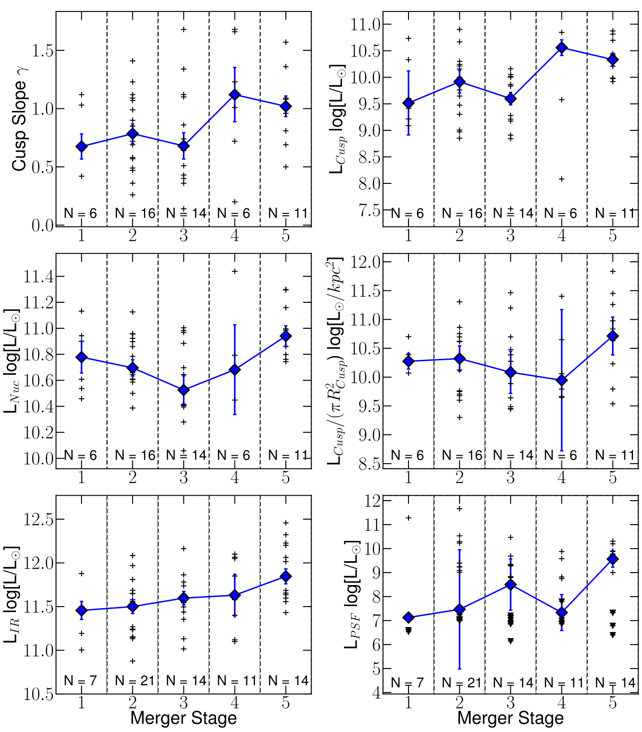

Figure 7. The cusp properties as a function of merger stage for all sources with $\gamma > 0.1$. Top left: the cusp slope (γ), top right: the cusp luminosity $L_{\rm Cusp}$, mid left: the total NIR luminosity within 1 kpc radius (excluding the central unresolved PSF component), mid right: the cusp surface density $L_{\rm cusp}/(\pi R_{\rm cusp}^2)$, bottom left: the total IR ($L_{\rm IR}$) luminosity of the galaxy, and bottom right: the luminosity of the central unresolved component (PSF). The number of sources in each merger stage bin is given at the bottom. The median values (with the standard error of the mean as blue error bar) are indicated with blue diamond markers and connected with a solid line.

on the cusp radius which is important to test since the cusp radius has in general larger systematic fit uncertainties than the cusp slope as shown in Section 4.7. Since $L_{\rm nuc}$ is defined within a 1 kpc radius, it is equivalent to the central surface-brightness density within a unit circle area of 1 kpc radius. The increase of total nuclear and cusp luminosity towards the late merger stage (MS5) is in agreement with the increase of the nuclear bulge density as shown in Haan et al. (2011a). Note that for all of these measurements the central unresolved component (PSF) has been excluded.

For completeness, we present in the bottom panel of Fig. 7 the luminosity of the unresolved component $L_{\rm PSF}$ and the luminosity $L_{\rm IR}$ of individual merger components as a function of merger stage for all our sources, both cusp and core galaxies. The median value of the luminosity of the unresolved component $L_{\rm PSF}$ (including also upper limits of non-PSF sources), which can be either an AGN or a very compact starburst, shows an increase of more than two orders of magnitude towards late merger stage, albeit with a large variation in each merger bin. The $L_{\rm IR}$ luminosity of the merger components shows an increase along the merger sequence, in particular at the late merger stage. These two findings are in agreement with previous studies of LIRGs which have indicated an increase of AGN activity and IR luminosity of the combined merger system along the merger sequence (e.g. Armus et al. 1989; Veilleux et al. 1995, 1997; Kim & Sanders 1998; Kim et al. 1998; Murphy et al. 1999, 2001).

4.6 Nuclear morphology of star formation: comparison with *HST* Paα emission line images

To investigate whether cusps are associated with a distinct SF morphology, such as nuclear SF rings or spirals, we have searched the *HST* archives for existing NIR, narrow-band images (much preferred over optical data due to nuclear dust effects). Four of our LIRGs have existing *HST* Paα imaging data, previously discussed in Alonso-Herrero et al. (2006). All of them exhibit a cusp with a slope $\gamma > 0.7$. Alonso-Herrero et al. (2006) classified the nuclear morphological Paα features as seen in their sample of 32 LIRGs into five categories: (a) compact (<1 kpc) nuclear Paα emission, (b) nuclear minispiral (inner 1–2 kpc), (c) nuclear star-forming rings, (d) large-scale (several kpc) Paα emission with H II regions located in the spiral arms and (e) large-scale Paα emission in highly inclined dusty systems. Since all overlapping galaxies have strong cusps, one might expect that all have the same morphological Paα features, i.e. if there is a direct relationship between the strength of cusp and the current SF morphology.

We find that all four galaxies have a strong Paα emission component on roughly the same scale as the cusp radius. Two galaxies (NGC 3256 and NGC 3690) show an additional extended Paα emission with H II regions located in the spiral arms. However, the morphology of the central Paα component ranges from concentrated Paα emission (NGC 3256 and NGC 3690) to nuclear star-forming ring (NGC 1614) and nuclear minispiral (MCG +12-02-001). This variety in morphology of the SF component (Paα emission) seems to be in agreement with recent VLT-SINFONI integral field spectroscopy observations of 17 (U)LIRGs (Piqueras López et al. 2012) which show a wide morphological variety in the ionized gas component while the warm molecular gas (H_2 emission) is highly concentrated in the nucleus. The similarity of the sizes of the central Paα emission and the stellar cusps indicate that, at least in these four LIRGs, ongoing SF may still be building cusps. Although the small number of sources for this study does not allow us to derive any decisive conclusions, the fact that no unique morphological SF feature can be associated with the stellar cups might suggest that either a larger range of nuclear SF morphologies and dynamical processes can build up a cusp, or that SF evolves through different morphological stages over the time-scale of the cusp formation. In particular, SF in the central region of NGC 1614 has been studied in detail using Brγ, H_2, Paα observations and NIR-to-MIR spectroscopy (e.g. Heisler et al. 1999; Alonso-Herrero et al. 2001; Kotilainen et al. 2001; Imanishi et al. 2010) which revealed a star-forming ring of ∼300–600 pc diameter around the nucleus with no evidence of AGN activity (Olsson et al. 2010). Väisänen et al. (2012) recently detected a broad inner ring of 3.3 μm PAH emission, suggesting an outward propagating ring of SF. A scenario of outward propagating SF would explain the lack of SF within the nuclear stellar cusp since most of the gas is likely already consumed or expelled from the inside of the stellar cusp. However, only a larger sample of high-resolution images of SF tracers and gas/stellar kinematics can answer in detail the question how the current SF and gas dynamics are linked to the build-up of the stellar cusp.

4.7 Spatial resolution dependences and unresolved components

It is important to test the robustness of our results against possible systematic biases in our measurements. The advantage of the GOALS LIRG sample is its completeness in terms of all-sky coverage and IR flux selection ($f_\nu(60\,\mu\rm m) \geq 5.24$ and $\log\,[L_{\rm IR}/{\rm L}_\odot] > 11.4$), being the largest sample of local LIRGs studied so far. However, some factors can possibly have an impact on the measured cusp properties, in particular AGN light contribution and finite spatial resolution.

The first case, AGN activity, might affect the observed NIR luminosity and hence one would expect a possible contribution to the measured cusp luminosity and slope. In principle, any point source (unresolved component) is taken into account by subtracting the *HST* pPSF from the images during the fitting process via GALFIT (see Section 3.2). Hence, a possible contribution of AGN activity to the cusp light is not very likely since the measured cusps are resolved (typical sizes of 100–500 pc) while the main dust heating by AGN (500–2000 K) is generated on scales of (10–100) pc (e.g. Soifer et al. 2001).

The second case, a spatial size dependency, is more difficult to rule out, since the spatial resolution and hence the scale on which the cusps are resolved, depends on the distance of the LIRGs (ranging from 30 to 350 Mpc for our sample). Given the small physical sizes of the nuclear cusps, it is important to verify that finite spatial resolution is not biasing our results. This is particularly important since more IR luminous LIRGs are typically found at larger distances than less luminous systems. In Fig. 8, we plot the cusp slope γ, the cusp break radius and the luminosity of the central unresolved component (PSF) as a function of distance for our sample. We cannot find any significant dependency as a function of the distance, indicating that distance related effects do not play a significant role statistically. Although this rules out a statistical dependence, we have also simulated directly how the nuclear slope would change as a function of distance for a representative set of LIRGs. The four LIRGs tested (NGC 3256, NGC 3690, NGC 2623 and UGC 12812) are all nearby (<100 Mpc), have no strong PSF component and display different cusp slopes (ranging from $\gamma = 0.2$ to $\gamma = 1.5$). We have smoothed and resized the images using a Gaussian beam and image regridding to simulate how these galaxies would appear at larger distances, changing both, their spatial resolution and angular size of the galaxies. After that we applied the same GALFIT procedure for each simulated galaxy to obtain the cusp parameters

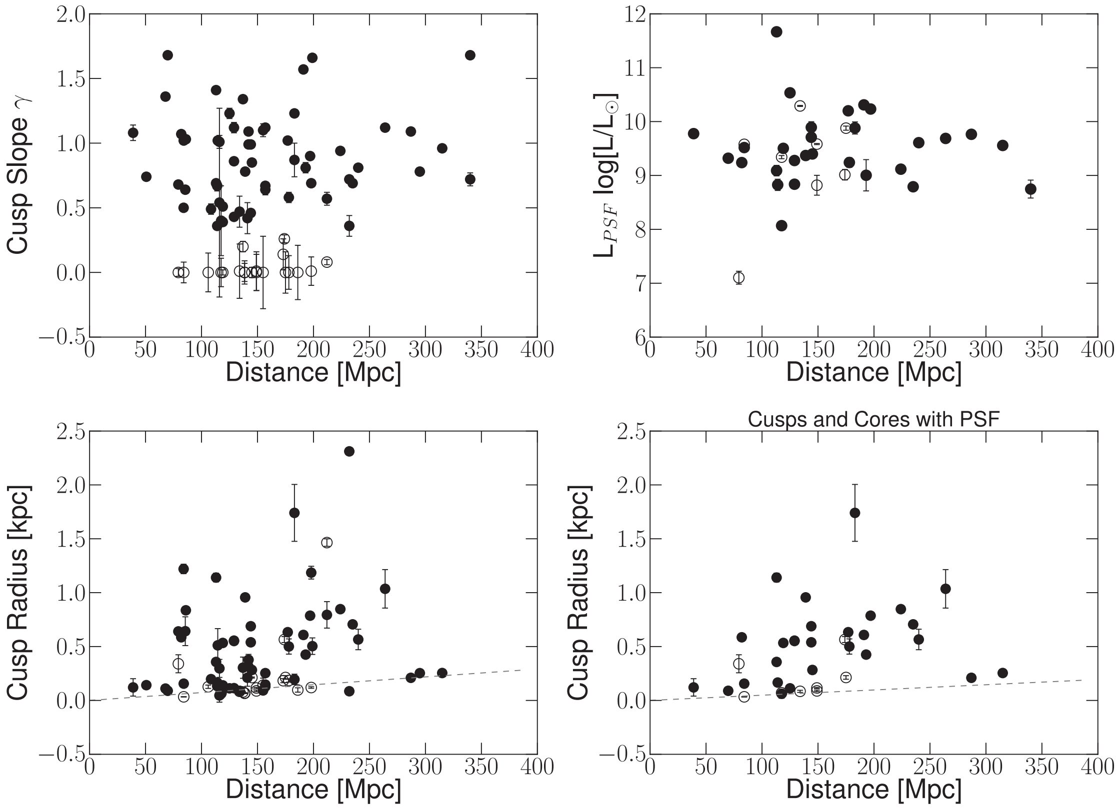

Figure 8. Nuker parameters as a function of distance to the LIRGs; top left: the cups slope (γ), top right: the central unresolved component (*HST* PSF), bottom left: the break radius, bottom right: the break radius for sources with a PSF. Cusps ($\gamma > 0.3$) and cores ($\gamma < 0.3$) are indicated with filled and open circle markers, respectively. The dashed line indicates the spatial resolution limit of the *HST*.

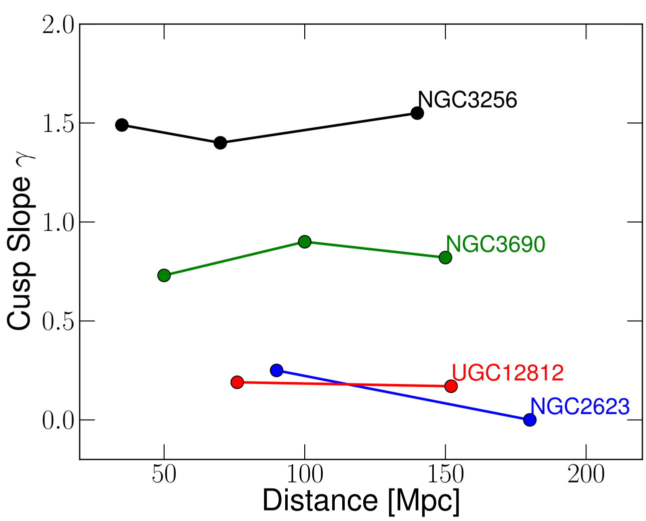

Figure 9. Systematic test of possible distance (resolution) dependences of the cusp slope parameter for four different galaxies. The GALFIT input images have been smoothed and resized in order to model the galaxies as they would appear at different distances.

as a function of distance. For consistency, we have fitted the same physical sky region for each simulation. As shown in Fig. 9, the cusp slope γ varies typically within a range of $\pm$(5–15 per cent) as a function of distance but no significant trend towards larger or smaller slopes with distance is found. The largest change appears for NGC 2623 from $\gamma = 0.25$ to $\gamma = 0.0$ if its distance were to double. The break radius is slightly more sensitive to the spatial resolution with changes of 10–50 per cent, but with no trend towards larger or smaller radius as a function of spatial resolution. These results show that the high, but limited spatial resolution of *HST* cannot cause us to detect cusps in our LIRGs where none exist, which is in accordance with our expectations.

On the contrary, if the cusp is unresolved, one would expect that its slope becomes flat ($\gamma = 0$) since the cusp excess light is already taken into account by the central PSF or it is just poorly constrained. For instance, in the case of a finite resolution limit, Lauer et al. (2007) have shown that a Nuker slope of $\gamma < 0.5$ can still have steep cusps if measured as the local slope at the resolution limit of the *HST*. Moreover, we cannot rule out that γ might be additionally suppressed by the PSF component. This implies that the cusp fraction and luminosity in our sample is a lower limit. This is relevant for studying a possible relationship between AGN and cusp light as discussed in Section 4.4 and is also important for the comparison to the slope in elliptical galaxies (see Section 5.4).

5 DISCUSSION

5.1 The formation of nuclear cusps: stellar masses and implication for SF time-scales

One of the main questions related to the formation of nuclear cusps is how much stellar mass is generated in the centre via gas dissipation. As shown in Section 4.2 we find a strong dependency between the total IR luminosity L_{IR} of a galaxy and its cusp NIR luminosity:

all galaxies above $\log [L_{\rm IR}/{\rm L}_\odot] = 11.9$ have cusp luminosities of $L_{\rm cusp} \gtrsim 10^{10}\,{\rm L}_\odot$ with an average value $L_{\rm cusp}/{\rm L}_\odot = [3.8 \pm 1.9] \times 10^{10}$, which is roughly five times larger than the average value of lower luminous LIRGs. Given our findings that all high-IR luminous galaxies are major mergers and that we see a similar increase of the cusp luminosity as a function of merger stage (from $L_{\rm cusp} \sim 1 \times 10^{10}\,{\rm L}_\odot$ to $3.2 \times 10^{10}\,{\rm L}_\odot$), we conclude that this increase in cusp luminosity $\Delta L_{\rm cusp}$ is very likely due to merger-induced gas dissipation building up a nuclear stellar cusp.

The average increase in cusp luminosity during a major merger ($\Delta\ L_{\rm cusp}$) is $\sim 2.5 \times 10^{10}\,{\rm L}_\odot$, which corresponds to a build-up of stellar mass $\langle \Delta M_{\rm cusp} \rangle$ of $(7 \pm 3.5) \times 10^9\,{\rm M}_\odot$ if we assume a standard mass-to-light ratio in the H band $\Upsilon_H = 0.3 \pm 0.15$. The applied Υ_H and its uncertainty is derived from STARBURST99 simulations (Leitherer et al. 1999) using Geneva High and Padova AGB tracks, Kroupa IMF, and instantaneous SF with a mass of $10^6\,{\rm M}_\odot$ and solar metallicity. The lower limit of $\Upsilon_H = 0.15$ is derived from the assumption that the NIR is dominated by young stars (4 Myr) while the upper limit of $\Upsilon_H = 0.45$ is a mix of young, intermediate (50 Myr), and old stellar populations (few 100 Myr) contributing equally to the NIR light. This ratio is consistent with (a) derived stellar masses of our LIRGs from SED fitting (U et al. 2012) using the models of Bruzual & Charlot (2003) and (b) recent estimates of dynamical masses obtained for the central 1 kpc in LIRGs (Hinz & Rieke 2006). For the latter case, we compared the total H-band luminosity (excluding central PSF) within the central 1 kpc in the five galaxies that overlap with the sample of Hinz & Rieke (2006) and assume that the dynamical mass in the centre is dominated by stars.

One important question is how long the current starburst will last. Merger simulations predict a strong starburst with a SFR of 50–500 ${\rm M}_\odot\ {\rm yr}^{-1}$ during the final coalescence of the two gas-rich nuclei (see e.g. Mihos & Hernquist 1994a; Combes & Melchior 2002; Springel & Hernquist 2005; Springel, Di Matteo & Hernquist 2005; Cox et al. 2008; Hopkins et al. 2008a; Bournaud et al. 2011). However, the predicted time-scales typically show a large variation and uncertainties (from 10 Myr to a few 100 Myr), depending on which model, initial conditions, gas fraction and feedback processes are used. We have shown in Section 4.5 that most of the cusp mass is built up between merger stage 3 (two nuclei in common envelope) and 4/5 (final coalescence of nuclei). This corresponds to an average time-scale of ∼500 Myr, which is based on the projected nuclear separation distance and mass ratios of the two merging galaxies (see Haan et al. 2011a).

Even so, it is possible that SF occurs in several bursts during this period. In principle, our observations should be able to provide important constraints given that the stellar cusp mass increase is equivalent to the integrated SFR over time during the late stages of a major merger. If we assume an average SFR during the final starburst phase when most of the mass of the cusp is built up, the time-scale of this starburst phase can be approximated by $t_{\rm SB} = \langle \Delta M_{\rm cusp} \rangle / \langle {\rm SFR}_{\rm SB} \rangle$. This assumption may not necessarily be valid for low IR luminosity LIRGs and non-mergers, which have smaller cusp luminosities and we cannot rule out the possibility that there is a significant cusp contribution that has formed at an earlier phase of their galaxy evolution. However, our cusp mass estimates are based on the most luminous galaxies in our sample (ULIRGs, $\log [L_{\rm IR}/{\rm L}_\odot] > 12.0$; note that cusp contribution of low-IR luminous galaxies is subtracted in $\Delta M_{\rm cusp}$) which are all major mergers at primarily their late stage and believed to build up most of the cusp mass during one major merger event with most of the remaining gas expelled or ionized.

The average SFR for our galaxies with $\log [L_{\rm IR}/{\rm L}_\odot] > 11.9$ (mean $\log [L_{\rm IR}/{\rm L}_\odot] = 12.1$) is $\sim 220\ {\rm M}_\odot\,{\rm yr}^{-1}$, which is based on the SFR–$L_{\rm IR}$ luminosity relation (Kennicutt 1998). We have applied a correction for extended $L_{\rm IR}$ emission, which is typically 50 per cent (Díaz-Santos et al. 2010, 2011), see also Section 4.4. Given $\langle \Delta M_{\rm cusp} \rangle$ of $(7 \pm 3.5) \times 10^9\,{\rm M}_\odot$ (see above) and assuming a constant SFR, we estimate an average time-scale for the final starburst phase of $\sim 60 \pm 30$ Myr to build up $\langle \Delta M_{\rm cusp} \rangle$. This is essentially the cusp doubling time-scale at the current SFR. Note that $\langle \Delta M_{\rm cusp} \rangle$ includes only the stellar cusp mass that is observed so far, which does not rule out any future SF fuelled by the remaining nuclear gas reservoir, which can be significant. On the other hand, if we average the SF over a time-scale of 500 Myr (from merger stage 3 to 4/5), when most of the cusp build-up occurs, we derive an average ${\rm SFR}_{500}$ of $\langle \Delta M_{\rm cusp} \rangle / t_{500} = (14 \pm 7)\ {\rm M}_\odot\,{\rm yr}^{-1}$.

5.2 On the nature of nuclear cusps in non-interacting LIRGs

One puzzling finding of this study is that all seven non-interacting LIRGs exhibit nuclear cusp light profiles, which is a slightly larger fraction than for interacting LIRGs (see Section 4.1). Although there are only seven non-interacting LIRGs in our sample, pre-merger LIRGs that show no interaction features (likely a mix between non-interacting and early stage mergers) also have a larger fraction of cusp galaxies than the mid- and late-stage mergers. However, even more interesting is that these non-interacting LIRGs have a significant cusp component at all and cusp luminosities similar to late-stage merger. In principle, there is no reason why these nuclear dissipational processes cannot occur in galaxies that are not participating in major mergers. However, the exact mechanism that leads to the central starburst and build-up of a cusp in these galaxies is still uncertain. Moreover, is the nuclear cusp formed during the current phase of SF or in a previous phase of SF due to an earlier merger event? If the latter is the case, an intriguing possibility is that the presence of a progenitor nuclear cusp may actually provide the physical conditions for the recent nuclear starburst which adds cusp mass through dissipation. One possibility would be that a progenitor cusp could provide the critical gravitational potential well to compress the gas and trigger instabilities in the gas that leads to dissipation and a starburst.

Other possible mechanisms might be minor mergers or secular evolution processes. Minor mergers can channel gas into the central region of a galaxy and may trigger a nuclear starburst, but with an efficiency that declines in approximately linear fashion with the mass ratio (Younger et al. 2007; Hopkins et al. 2008b). Secular evolution processes are suggested to build up pseudo-bulges and dense central concentrations of gas and SF due to bar or oval stellar distribution which exert gravitational torques on the gas and might trigger gas inflow (see e.g. Laurikainen & Salo 2002; García-Burillo et al. 2005; Boone et al. 2007; Haan et al. 2009). However, measurements of local disc galaxies show that these structures evolve on much larger time-scales of a few billion years at nuclear SFRs at least one order of magnitude below the low IR luminosity end of LIRGs (for a review see Kormendy & Kennicutt 2004). Even so, none of the non-interacting galaxies in our sample, except IC 5298, has a strong bar based on its optical and NIR light distribution. Our multiwavelength *HST* images show that most of these galaxies (e.g. MCG-03-04-014, NGC 695, VII Zw 031, IC 5298) have non-disturbed discs with strong dust and stellar spiral arms from the outer disc to the very centre.

We can also rule out the scenario that most of the apparent non-interacting LIRGs are in a more quiescent post-merger phase where stellar tidal tails and streams have faded away: merger simulations (e.g. Hernquist 1993; Hernquist, Heyl & Spergel 1993; Springel et al. 2005; Cox et al. 2008; Wang et al. 2012) have shown that tidal tails in major mergers remain typically present (luminosity >1 per cent of disc) until >10 dynamical time-scales (corresponding to a post-merger time-scale of ≥2 Gyr). The fact that tidal tails are not fading away quickly after the coalescence of the nuclei is supported by our *HST* observations in the optical light which show no significant decrease of the ratio of tidal features to disc light (Kim et al. 2013). In contrast, the post-starburst time-scale is expected to last only a few dynamical time-scales, much shorter than the time-scale until tidal tails fade away.

5.3 Increasing compactness along the merger sequence – comparison to high-redshift studies

Recent deep high-resolution ground- and space-based surveys have revealed that a significant fraction of massive galaxies at $z > 1$ is surprisingly compact (e.g. Daddi et al. 2005; Trujillo et al. 2006, 2007; Cimatti et al. 2008; Franx et al. 2008; Damjanov et al. 2009; Targett et al. 2011) with effective radii well below the local galaxy size–mass relation. Within the last three years even deeper observations (in particular CANDELS survey) provided mounting evidence for the truly compact nature of many high-redshift galaxies (van Dokkum et al. 2010; Bruce et al. 2012; Chevance et al. 2012; Kartaltepe et al. 2012; Ryan et al. 2012; Szomoru, Franx & van Dokkum 2012). In particular Bruce et al. (2012) have decomposed the structure of the most massive galaxies (∼200 galaxies) in the CANDELS-UDS field (*HST F*160-band images) with photometric redshifts $1 < z < 3$ using single Sérsic and bulge/disc models. This study finds that in particular bulge-dominated objects show evidence for a growing bimodality in the size–mass relation with increasing redshift. The fraction of bulges consistent with the local size–mass relation is 10–25 per cent at $1 < z < 3$ and compact bulges have effective radii a factor of roughly 4 smaller at $z > 2$ than local ellipticals of comparable mass. In the local Universe such massive galaxies are primarily bulge dominated, while galaxies at higher redshift ($z > 2$) tend to be more disc dominated.

Given the argument that LIRGs are very abundant and dominate the total IR energy density emitted at redshifts of $1 < z < 3$ (Elbaz et al. 2002; Le Floc'h et al. 2005; Bridge et al. 2007; Caputi et al. 2007; Magnelli et al. 2009; Berta et al. 2011), a possible link between the morphological evolution of galaxies during their LIRG phase and the compactness of galaxies observed at high-z might be suggestive. As shown in recent merger simulations by Hopkins et al. (2008b) a gas inflow of ∼10 per cent of the total gas shrinks the effective bulge radius to about half its previous size and subsequently enhances the bulge surface brightness. Haan et al. (2011a) have shown that the effective bulge radius decreases about a factor of 2.5, on average, from non-interacting/early stage to mid-stage merger and again a factor of 2.2 from mid-stage to early stage merger. The bulge surface brightness increases on average about a factor of 5 from non-interacting/early stage to mid-stage merger and a factor of 10 from mid-stage to late-stage merger. In this study, we confirm the increase in compactness given the increase of the nuclear surface density within 1 kpc (which is independent from bulge or cusp radius) and cusp surface density about a factor of 2 from early/mid-stage to late-stage merger. Note that the unresolved component has been already subtracted in all our studies. This suggests that both components of a merger remnant, one formed through violent relaxation of progenitor stars (dissipationless, spheroid, see Haan et al. 2011a) and the other through gas dissipation (cusp; see density in Fig. 7), become more compact towards the late merger stage due to gas infall. Whether triggered by major mergers or by other instabilities, a large gas infall and nuclear starbursts are also expected in high-z galaxies, which might be a possible explanation for the dramatic increase in compactness in these sources.

5.4 Are LIRGs evolving into elliptical galaxies: comparison of nuclear properties as tracer of their evolutionary linkage

One important question is what fraction of present day ellipticals could be formed by gas-rich major mergers that have local gas fractions? The picture that mergers transform disc galaxies into massive elliptical and S0 galaxies is often suggested by observations based on the comparisons of the large-scale appearance (at radii of several kpc) of the radial light profile of old merger remnants with those of ellipticals (e.g. Wright et al. 1990; James et al. 1999; Genzel et al. 2001; Tacconi et al. 2002; Rothberg & Joseph 2004). However, the end result of a major merger may depend on several factors such as merger-mass ratio, gas fraction and feedback processes due to supernovae or AGN activity (e.g. Bournaud, Jog & Combes 2005; Springel & Hernquist 2005; Robertson et al. 2006). Even so, fitting the large-scale profile of ongoing and recent major mergers is often not possible since the stellar distribution is still dominated by violent relaxation. This is not the case for merger nuclei which undergo a much more rapid relaxation due to the decrease of the dynamical time-scale with smaller radial distance from the centre of a galaxy. Early-type galaxies show a strong bimodality: cusp elliptical galaxies are relatively faint in optical light, rotate rapidly, have discy isophotes, host radio-quiet AGN and do not contain large amounts of X-ray-emitting gas; core elliptical galaxies are brighter in the optical, rotate slowly, have boxy isophotes, radio-loud AGN and diffuse X-ray emission. For a summary of these observational findings see Kormendy et al. (2009), Silk & Norman (2009), Nipoti (2010), and references therein. This dichotomy suggests that core and cusp ellipticals went through different evolutionary processes. Here, we compare for the first time the cusp and core properties in the few remaining gas-rich major mergers still present in the local Universe to those of present-day core and cusp-dominated ellipticals.

We have chosen the sample of Lauer et al. (2007) as a reference sample of early-type galaxies to which we compare the cusp properties of our LIRG sample. The sample compiled by Lauer et al. (2007) is the largest sample of 219 early-type galaxies and has been derived by homogenizing a variety of studies (Lauer et al. 1995; Faber et al. 1997; Quillen et al. 2000; Ravindranath et al. 2001; Rest et al. 2001; Laine et al. 2003; Lauer et al. 2005), primarily observed in *V* and *H* band. Even though that this sample combines optical and NIR observations, it is unlikely that this affects the nuclear slope γ because Seigar et al. (2002) have found that the NIR structural properties and γ parameter of spiral galaxies are very similar to those obtained in the optical wavelength region for the same systems. Note that elliptical galaxies must be even less affected by any colour-dependence of γ than spiral galaxies, which usually show more local colour variations. The Lauer et al. (2007) sample is the best match to our analysis because (1) all observations are taken with *HST* at high angular resolution, (2) the cusp parameters are derived using the Nuker law parameters and (3) it overlaps with the host galaxies luminosity and distance range of our LIRG sample. For the hosts magnitude, we have taken the catalogued 2MASS flux *H* band which is a fair proxy of the stellar mass of the galaxies and is not biased by dust extinction. The 2MASS *K*

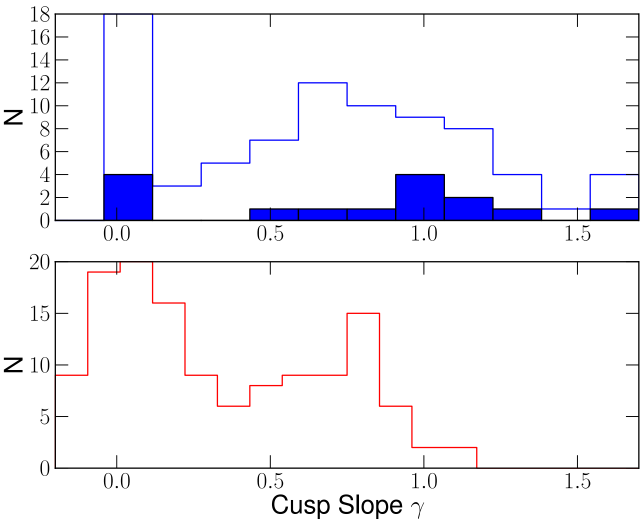

Figure 10. Histogram of the Nuker gamma parameter for LIRGs (top panel) and early-type galaxies (bottom panel; sample from Lauer et al. 2007) within the same total luminosity range ($-25.5 < M_H < -22.5$). Late-stage mergers are indicated as filled histogram in the top panel.

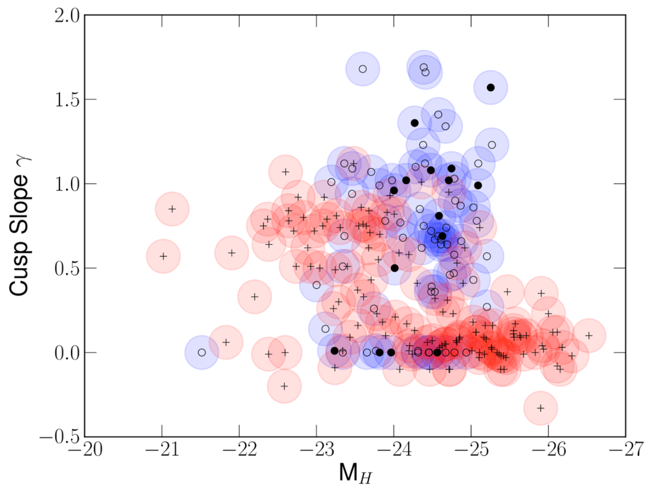

Figure 11. Overview of the Nuker gamma parameter as a function of the total absolute H-band magnitude (2MASS). While early-type galaxies (red, plus marker; Lauer et al. 2007) show a strong dependence of the presence of cusp and cores as a function of host magnitude, LIRGs (blue, circle marker) do not follow this trend and represent a distinct population. Late-stage mergers are indicated with a filled circle.

Table 4. Comparison of absolute host H-band magnitude between LIRGs and ellipticals.

	LIRGs	Ellipticals
Median (mean) M_H cusps:	−24.5 (−24.4)	−23.5 (−23.5)
Median (mean) M_H cores:	−24.3 (−24.0)	−25.1 (−24.9)

band might be less affected by red supergiants, but has likely more contribution from warm dust emission and is by far not as sensitive in magnitude as the H band. Using the catalogued 2MASS values rather than converting the visible magnitudes in Lauer et al. (2007) and our measured H-band fluxes, we can ensure that the comparison between both samples is not biased by instrumental and measurement method and includes only the galaxies within the same mass range. Moreover, we have applied a distance cut of >20 Mpc for the Lauer sample, which sorts out most of the small galaxies which are not in the mass range of the LIRGs ($M_H > -21$). The mean H-band absolute magnitude is very similar with −24.27 and −24.29 mag for the Lauer et al. (2007) and LIRG sample, respectively. For consistency, we have compared the optical magnitudes measured by Lauer et al. (2007) with the catalogued 2MASS H-band magnitudes within our magnitude range and found a very good linear relation.

In Fig. 10, we compare the cusp slope (γ) distribution between LIRGs and ellipticals averaged over the same magnitude range. This comparison reveals the following: within the $-23 < M_H < -25.5$ range, which contains more than 98 per cent of the LIRGs in our sample, we find a significantly larger ratio of cusp ($\gamma > 0.3$) to core ($\gamma < 0.3$) galaxies for LIRGs (cusp/core ≥ 3.2) than for early-type galaxies (cusp/core ≈ 0.7). This means that at least 76 per cent of LIRGs are cusp sources while only 41 per cent of early-type galaxies harbour cusps within the same magnitude range. The mean and median values of the host absolute magnitude M_H for both samples are given in Table 4. The difference between LIRGs and ellipticals is likely larger since there might be a significant fraction of cusps unresolved with NICMOS (resolution of 0.15 arcsec in comparison to 0.05 arcsec for WFPC2 in $F555W$) and subsequently taken into account by the PSF component that is fitted with GALFIT.

In Fig. 11, we compare γ as a function of the host absolute magnitude M_H between LIRGs and early-type galaxies. The strong dependence of γ in early-type galaxies on visible magnitude (Lauer et al. 2007) is also apparent in the NIR (H band). However, LIRGs do not follow this trend and form a clearly distinct population in the $M_H-\gamma$ diagram: most of the LIRGs with cusps have larger H-band luminosities (on average one order of magnitude) than cusp ellipticals. The distribution of LIRGs in the $M_H-\gamma$ diagram does not depend on whether they are non-merger, early stage merger or late-stage merger, with the exception that all non-merger LIRGs are cusp galaxies (as already pointed out in Section 4.5). Moreover, the distribution seems also not to depend on the variation in spatial resolution (i.e. we find a similar distribution if only LIRGs are taken into account with distances of less than 100 Mpc). This means for most of the LIRGs for which we found a cusp, we would have expected to find a core given the galaxies' luminosity and distribution of ellipticals.

One intuitive explanation for the significantly larger cusp fraction in LIRGs than in elliptical galaxies would be the destruction of cusps after the LIRG phase has passed. If this would be the case a significant fraction of cusp LIRGs would evolve into massive core galaxies since the host mass of cusp LIRGs and core ellipticals is roughly the same. Regarding Fig. 10, this would mean that half of cusp LIRGs would move down in cusp slope to end up as core ellipticals. However, destruction or flattening of the nuclear stellar cusp cannot be easily accomplished without any major disruption. Theoretical models predict that nuclear stellar cusps remain preserved in the central light profile of a galaxy during a wet merger event (Hopkins et al. 2009b). In particular, cusp destruction via massive BH binaries has been proposed, but it can only remove a stellar mass of the order of the combined BH mass (see e.g. Merritt & Milosavljević 2005 for a review), which is much smaller than the cusp masses in our sample. In late-stage LIRGs the mean cusp mass is $\sim 3 \times 10^{10}$ $L_\odot$ versus a mean bulge mass of $\sim 15 \times 10^{10}$ $L_\odot$ in the H band (see Haan et al. 2011a); the BH mass is ∼400 times smaller than the bulge mass estimated by the H-band luminosity (Marconi & Hunt

2003). Therefore, either cusp destruction via BH binaries is much more efficient (mass removal of at least 10 times the combined BH mass) than previously assumed or another mechanism destroys the cusp after the LIRG phase has passed.

One mechanism that could possibly lead to a strong reduction of the cusp and the formation of a core is a gas-poor ('dry') merger of two cusp galaxies (see Lauer et al. 2007; Hopkins et al. 2009b; Kormendy et al. 2009). Indeed observations of elliptical galaxies have shown evidence for a correlation between a central stellar light deficit $L_{\rm def}$ in core ellipticals with the mass of the central stellar BH and the bulge velocity dispersion of their host galaxies (Kormendy & Bender 2009), suggesting that cores are scoured by BH binaries. Interestingly, this study does not find any correlation between BH mass and the excess light in cusp ellipticals, which suggests that scouring by BH binaries is only efficient in dry (gas-poor) mergers, which are believed to form core ellipticals, and not in wet (gas-rich) mergers that form nuclear cusps. Given our results, this would imply that most LIRGs in the early Universe must have experienced two subsequent evolutionary processes before they could end up as core ellipticals: first, most of their gas must have been expelled, and secondly, they must have been involved in at least one more major merger event with another gas-poor galaxy. The fact that present-day massive ellipticals have primarily cores suggests that these two steps, gas ejection and subsequent gas-poor remerger, must have happened during a very short episode in cosmic time since a long-term evolution would have led to a mix with gas-rich galaxies and could not have destroyed their cusps efficiently.

Another scenario would be that SF was quickly shut down in gas-rich galaxies (e.g. due to feedback from supernovae, hot stars and AGN) before gas could accumulate in the very centre of massive ellipticals, which would prevent a central cusp from forming and build up a stellar core distribution instead. The reason that these feedback processes are less strong in today's LIRGs may lie in the fact that gas fractions and merger densities were much higher at cosmic times when most massive ellipticals formed than in local LIRGs. Evidence that the cusp build-up might stop in some galaxies before the final coalescence of the nuclei comes from a detailed multiwavelength study of Markarian 266 (Mazzarella et al. 2012, here named NGC 5256 north and south;) which has two AGN with kiloparsec-scale separation and shows evidence that the dust outflow phase can begin in an LIRG well before the galaxies fully coalesce.

Not only massive core ellipticals, but also most cusp ellipticals are not remnants of gas-rich major mergers like the local LIRG population, which are on average one order of magnitude more luminous in the NIR light (i.e. more massive) than cusp ellipticals. One possible explanation for this mass discrepancy is that cusp ellipticals formed at an early phase of our Universe when most galaxies were smaller and have not reached the masses as observed for today's gas rich major mergers. Once formed, these cusp ellipticals must have not gained significant mass via subsequent merger, unlike core ellipticals which likely evolved through several subsequent dry merger events. The reason why we find almost no cusp LIRGs today at smaller masses could be possibly explained by the fact that galaxies in the early Universe had significantly larger gas fractions, eventually enabling them to reach critical gas pressure rates and instabilities to trigger central starbursts at much smaller host galaxy masses.

6 SUMMARY

The formation of nuclear stellar cusps requires powerful compact starbursts, which makes (U)LIRGs one of the most representative galaxy population for studying the actual formation of cusps in extreme starburst galaxies. We have analysed the nuclear stellar structure and cusp properties using 2D fitting of the Nuker profile for a complete sample of 85 (U)LIRGS (with $11.4 < \log\,[L_{\rm IR}/{\rm L}_{\odot}] < 12.5$) in the GOALS sample based on *HST* NIR imaging, and have applied MIR diagnostics for AGN/starburst characterization and SFR estimations. The main results are summarized as follows.

(i) Nuclear stellar cusps are resolved in 76 per cent of (U)LIRGs while the remaining 24 per cent have flat nuclear profiles (core galaxies) with nuclear slopes <0.3. The cusp strength and luminosity increase with far-IR luminosity (excluding AGN), confirming models that recent starburst activity is associated with the build-up of stellar cusps. In particular, all galaxies above $\log\,[L_{\rm IR}/{\rm L}_{\odot}] = 11.9$ have cusp luminosities of ($L_{\rm cusp} \gtrsim 10^{10}\,{\rm L}_{\odot}$) with an average value $L_{\rm cusp}/{\rm L}_{\odot} = [3.8 \pm 1.9] \times 10^{10}$, which is roughly five times larger than for lower IR luminous galaxies ($\log\,[L_{\rm IR}/{\rm L}_{\odot} \sim 11.5]$). An average increase in cusp luminosity $\Delta L_{\rm cusp} \sim 2.5 \times 10^{10}\,{\rm L}_{\odot}$ is found as a function of far-IR luminosity and merger stage, which corresponds to a build-up of stellar mass $\Delta M_{\rm cusp}$ of $(7 \pm 3.5) \times 10^{9}\,{\rm M}_{\odot}$. Most of the cusp build-up seems to occur within a few 100 Myr during the final coalescence of the nuclei. If we assume that most of the cusp mass is built up during one starburst, a time-scale of $\sim$60 $\pm$ 30 Myr would be required based on the average SFR in (U)LIRGs.

(ii) The nuclear stellar surface-brightness profiles of local (U)LIRGs are very different from those of present day's early-type galaxies with comparable masses. Our comparison between (U)LIRGs and a large sample of local elliptical galaxies (within the same host galaxy mass range) reveals (a) a significant larger cusp/core ratio in (U)LIRGs ($\gtrsim$3.2:1) than in ellipticals ($\lesssim$0.7:1) and (b) (U)LIRGs do not follow the cusp to core dependency of ellipticals as a function of host galaxy mass ($M_H - \gamma$ diagram) and clearly represent a distinct population. The majority of the cusp (U)LIRGs have on average host luminosities similar to core ellipticals, which is one order in magnitude larger than for cusp ellipticals. Moreover, gas-rich late-stage mergers show no indications of a cusp destruction by BH-binary scouring during the coalescence of their nuclei. These results suggest that the progenitors of present day's massive ellipticals must have either expelled most of their gas during a brief episode in cosmic time and destroyed their cusps in subsequent gas-poor remerger events, or that SF was quickly shut down before gas could efficiently accumulate in the very centre to build up a cusp (e.g. via feedback from supernovae, hot stars and AGN due to higher gas fractions at high-z). The reason why there are almost no cusp LIRGs observed at smaller masses could be possibly explained by the fact that galaxies in the early Universe had significantly larger gas fractions, eventually enabling them to reach critical gas pressure rates and instabilities to trigger central starbursts at much smaller host galaxy masses.

(iii) With increasing cusp strength and luminosity along the merger process, the nuclear structure becomes more compact which is observed as an increasing cusp surface density (factor of 5–10) and total nuclear surface density within a radius of 1 kpc (factor of 4–5). This result is in agreement with the significant increase of the bulge surface density shown in Haan et al. (2011a), suggesting that both components of a merger remnant, one formed through violent relaxation of progenitor stars (dissipationless, spheroid) and the other through gas dissipation (cusp), become more compact towards the late merger stage due to gas infall, which might be a possible explanation for the dramatic increase in bulge compactness in high-redshift studies (e.g. CANDELS).

(iv) Comparison of the nuclear structure in four cusp LIRGs observed in the *HST H*-band to corresponding *HST* Paα emission line images reveals that the Paα emission has various morphologies (nuclear star-forming rings, nuclear minispiral and concentrated emission), suggesting that there is apparently no single morphological SF feature associated with the build-up of cusps. However, all four galaxies have a strong Paα emission component with roughly the same size as the cusp, which demonstrates that the current SF is still linked up with the build-up of the cusp.

(v) Evidence for ultracompact nuclear starbursts is found in $\sim$13 per cent of LIRGs, which have a strong unresolved central light component but no significant evidence of an AGN.

ACKNOWLEDGEMENTS

The authors wish to thank Robert Joseph for a careful review of the manuscript and many valuable suggestions to improve this paper. The authors are very grateful to Tod R. Lauer for helpful discussions on the characterization of cusp and cores and the comparison between LIRGs and elliptical galaxies. This research has made use of the NASA/IPAC Extragalactic Database (NED) and the Infrared Science Archive (IRSA) which are operated by the Jet Propulsion Laboratory, California Institute of Technology, under contract with the National Aeronautics and Space Administration. Support for this work was provided through grant *HST* GO 11235.01-A by NASA from the Space Telescope Science Institute, which is operated by the Association of Universities for Research in Astronomy, Inc., under NASA contract NAS 5-26555. VC would like to acknowledge partial support from the EU FP7 grant PIRSES-GA-2012-316788. LA and DBS acknowledge the hospitality of the Aspen Center for Physics, which is supported by the National Science Foundation grant no. PHY-1066293.

REFERENCES

Alonso-Herrero A., Engelbracht C. W., Rieke M. J., Rieke G. H., Quillen A. C., 2001, ApJ, 546, 952
Alonso-Herrero A., Rieke G. H., Rieke M. J., Colina L., Pérez-González P. G., Ryder S. D., 2006, ApJ, 650, 835
Armus L., Heckman T. M., Miley G. K., 1989, ApJ, 347, 727
Armus L. et al., 2007, ApJ, 656, 148
Armus L. et al., 2009, PASP, 121, 559
Barnes J. E., Hernquist L., 1992, ARA&A, 30, 705
Bender R., 1988, A&A, 193, L7
Berta S. et al., 2011, A&A, 532, A49
Boone F. et al., 2007, A&A, 471, 113
Bournaud F., Jog C. J., Combes F., 2005, A&A, 437, 69
Bournaud F. et al., 2011, ApJ, 730, 4
Bridge C. R. et al., 2007, ApJ, 659, 931
Bruce V. A. et al., 2012, MNRAS, 427, 1666
Bruzual G., Charlot S., 2003, MNRAS, 344, 1000
Buitrago F., Trujillo I., Conselice C. J., Bouwens R. J., Dickinson M., Yan H., 2008, ApJ, 687, L61
Cappellari M. et al., 2007, MNRAS, 379, 418
Caputi K. I. et al., 2007, ApJ, 660, 97
Charmandaris V., Stacey G. J., Gull G., 2002, ApJ, 571, 282
Charmandaris V., Le Floc'h E., Mirabel I. F., 2004, ApJ, 600, L15
Chevance M., Weijmans A.-M., Damjanov I., Abraham R. G., Simard L., van den Bergh S., Caris E., Glazebrook K., 2012, ApJ, 754, L24
Cimatti A. et al., 2008, A&A, 482, 21
Combes F., Melchior A. L., 2002, Ap&SS, 281, 383
Côté P. et al., 2007, ApJ, 671, 1456
Cox T. J., Jonsson P., Somerville R. S., Primack J. R., Dekel A., 2008, MNRAS, 384, 386
Crane P. et al., 1993, AJ, 106, 1371
Daddi E. et al., 2005, ApJ, 626, 680
Damjanov I. et al., 2009, ApJ, 695, 101
Davies R. L., Illingworth G., 1983, ApJ, 266, 516
Desai V. et al., 2007, ApJ, 669, 810
Díaz-Santos T. et al., 2010, ApJ, 723, 993
Díaz-Santos T. et al., 2011, ApJ, 741, 32
Díaz-Santos T. et al., 2013, ApJ, in press
Elbaz D., Cesarsky C. J., Chanial P., Aussel H., Franceschini A., Fadda D., Chary R. R., 2002, A&A, 384, 848
Emsellem E. et al., 2007, MNRAS, 379, 401
Faber S. M. et al., 1997, AJ, 114, 1771
Ferrarese L., van den Bosch F. C., Ford H. C., Jaffe W., O'Connell R. W., 1994, AJ, 108, 1598
Ferrarese L. et al., 2006, ApJS, 164, 334
Franx M., van Dokkum P. G., Schreiber N. M. F., Wuyts S., Labb I., Toft S., 2008, ApJ, 688, 770
García-Burillo S., Combes F., Schinnerer E., Boone F., Hunt L. K., 2005, A&A, 441, 1011
Gebhardt K. et al., 1996, AJ, 112, 105
Genzel R. et al., 1998, ApJ, 498, 579
Genzel R., Tacconi L. J., Rigopoulou D., Lutz D., Tecza M., 2001, ApJ, 563, 527
Graham A. W., 2012, ApJ, 746, 113
Graham A. W., Guzmán R., 2003, AJ, 125, 2936
Haan S., Schinnerer E., Emsellem E., Garca-Burillo S., Combes F., Mundell C. G., Rix H.-W., 2009, ApJ, 692, 1623
Haan S. et al., 2011a, AJ, 141, 100
Haan S. et al., 2011b, ApJS, 197, 27
Heisler C. A., Dopita M. A., Kewley L. J., Lumsden S. L., 1999, Ap&SS, 266, 181
Hernquist L., 1993, ApJ, 409, 548
Hernquist L., Heyl J. S., Spergel D. N., 1993, ApJ, 416, L9
Hinz J. L., Rieke G. H., 2006, ApJ, 646, 872
Hopkins P. F., Hernquist L., Cox T. J., Kereš D., 2008a, ApJS, 175, 356
Hopkins P. F., Hernquist L., Cox T. J., Dutta S. N., Rothberg B., 2008b, ApJ, 679, 156
Hopkins P. F., Cox T. J., Hernquist L., 2008c, ApJ, 689, 17
Hopkins P. F., Cox T. J., Dutta S. N., Hernquist L., Kormendy J., Lauer T. R., 2009a, ApJS, 181, 135
Hopkins P. F., Lauer T. R., Cox T. J., Hernquist L., Kormendy J., 2009b, ApJS, 181, 486
Hopkins P. F., Murray N., Quataert E., Thompson T. A., 2010, MNRAS, 401, L19
Howell J. et al., 2010, ApJ, 715, 572
Imanishi M., Nakagawa T., Shirahata M., Ohyama Y., Onaka T., 2010, ApJ, 721, 1233
Inami H. et al., 2010, AJ, 140, 63
Jaffe W., Ford H. C., O'Connell R. W., van den Bosch F. C., Ferrarese L., 1994, AJ, 108, 1567
James P., Bate C., Wells M., Wright G., Doyon R., 1999, MNRAS, 309, 585
Kartaltepe J. S. et al., 2012, ApJ, 757, 23
Kennicutt R. C., Jr, 1998, ApJ, 498, 541
Kim D.-C., Sanders D. B., 1998, ApJS, 119, 41
Kim D.-C., Veilleux S., Sanders D. B., 1998, ApJ, 508, 627
Kim D.-C. et al., 2013, ApJ, 768, 102
Kormendy J., Bender R., 2009, ApJ, 691, L142
Kormendy J., Sanders D. B., 1992, ApJ, 390, L53
Kormendy J., Kennicutt R. C., Jr, 2004, ARA&A, 42, 603
Kormendy J., Fisher D. B., Cornell M. E., Bender R., 2009, ApJS, 182, 216
Kotilainen J. K., Reunanen J., Laine S., Ryder S. D., 2001, A&A, 366, 439
Krist J. E., Hook R. N., 1997, in Casertano S. et al., eds, HST Calibration Workshop with a New Generation of Instruments. STScI, Baltimore, p. 192
Laine S., van der Marel R. P., Lauer T. R., Postman M., O'Dea C. P., Owen F. N., 2003, AJ, 125, 478

Lauer T. R. et al., 1992, AJ, 104, 552
Lauer T. R. et al., 1995, AJ, 110, 2622
Lauer T. R. et al., 2005, AJ, 129, 2138
Lauer T. R. et al., 2007, ApJ, 664, 226
Laurikainen E., Salo H., 2002, MNRAS, 337, 1118
Lee J. C., Hwang H. S., Lee M. G., Kim M., Lee J. H., 2012, ApJ, 756, 95
Le Floc'h E. et al., 2005, ApJ, 632, 169
Le Floc'h E., Charmandaris V., Gordon K., Forrest W. J., Brandl B., Schaerer D., Dessauges-Zavadsky M., Armus L., 2012, ApJ, 746, 7
Leitherer C. et al., 1999, ApJS, 123, 3
Magnelli B., Elbaz D., Chary R. R., Dickinson M., Le Borgne D., Frayer D. T., Willmer C. N. A., 2009, A&A, 496, 57
Marconi A., Hunt L. K., 2003, ApJ, 589, L21
Mazzarella J. M. et al., 2012, AJ, 144, 125
Merritt D., Milosavljević M., 2005, Living Rev. Relativ., 8, 8
Mihos J. C., Hernquist L., 1994a, ApJ, 431, L9
Mihos J. C., Hernquist L., 1994b, ApJ, 437, L47
Mirabel I. F. et al., 1998, A&A, 333, L1
Murphy T. W., Jr, Soifer B. T., Matthews K., Kiger J. R., Armus L., 1999, ApJ, 525, L85
Murphy T. W., Jr, Soifer B. T., Matthews K., Armus L., 2001, ApJ, 559, 201
Naab T., Ostriker J. P., 2009, ApJ, 690, 1452
Nipoti C., 2010, in Antonuccio-Delogu V., Silk J., eds, AGN Feedback in Galaxy Formation. Cambridge Univ. Press, Cambridge, p. 194
Olsson E., Aalto S., Thomasson M., Beswick R., 2010, A&A, 513, A11
Peng C. Y., Ho L. C., Impey C. D., Rix H.-W., 2010, AJ, 139, 2097
Petric A. O. et al., 2011, ApJ, 730, 28
Piqueras López J., Colina L., Arribas S., Alonso-Herrero A., Bedregal A. G., 2012, A&A, 546, A64
Quillen A. C., Bower G. A., Stritzinger M., 2000, ApJS, 128, 85
Ravindranath S., Ho L. C., Peng C. Y., Filippenko A. V., Sargent W. L. W., 2001, AJ, 122, 653
Rest A., van den Bosch F. C., Jaffe W., Tran H., Tsvetanov Z., Ford H. C., Davies J., Schafer J., 2001, AJ, 121, 2431
Robertson B., Cox T. J., Hernquist L., Franx M., Hopkins P. F., Martini P., Springel V., 2006, ApJ, 641, 21
Rothberg B., Joseph R. D., 2004, AJ, 128, 2098
Ryan R. E., Jr et al., 2012, ApJ, 749, 53
Sanders D. B., Mirabel I. F., 1996, ARA&A, 34, 749
Sanders D. B., Mazzarella J. M., Kim D.-C., Surace J. A., Soifer B. T., 2003, AJ, 126, 1607
Scoville N. Z. et al., 2000, AJ, 119, 991
Sérsic J. L., 1968, Atlas de Galaxias Australes. Observatorio Astronomico, Cordoba, Argentina
Seigar M., Carollo C. M., Stiavelli M., de Zeeuw P. T., Dejonghe H., 2002, AJ, 123, 184
Silk J., Norman C., 2009, ApJ, 700, 262
Soifer B. T. et al., 2001, AJ, 122, 1213
Springel V., Hernquist L., 2005, ApJ, 622, L9
Springel V., Di Matteo T., Hernquist L., 2005, MNRAS, 361, 776
Stierwalt S. et al., 2013, ApJS, 206, 1
Sturm E., Lutz D., Tran D., Feuchtgruber H., Genzel R., Kunze D., Moorwood A. F. M., Thornley M. D., 2000, A&A, 358, 481
Surace J. A., 1998, PhD thesis, University of Hawaii
Surace J. A., Sanders D. B., Vacca W. D., Veilleux S., Mazzarella J. M., 1998, ApJ, 492, 116
Szomoru D., Franx M., van Dokkum P. G., 2012, ApJ, 749, 121
Tacconi L. J., Genzel R., Lutz D., Rigopoulou D., Baker A. J., Iserlohe C., Tecza M., 2002, ApJ, 580, 73
Targett T. A., Dunlop J. S., McLure R. J., Best P. N., Cirasuolo M., Almaini O., 2011, MNRAS, 412, 295
Trujillo I. et al., 2006, MNRAS, 373, L36
Trujillo I., Conselice C. J., Bundy K., Cooper M. C., Eisenhardt P., Ellis R. S., 2007, MNRAS, 382, 109
U V. et al., 2012, ApJS, 203, 9
Väisänen P., Rajpaul V., Zijlstra A. A., Reunanen J., Kotilainen J., 2012, MNRAS, 420, 2209
van der Wel A., Holden B. P., Zirm A. W., Franx M., Rettura A., Illingworth G. D., Ford H. C., 2008, ApJ, 688, 48
van Dokkum P. G. et al., 2010, ApJ, 709, 1018
Veilleux S., Kim D.-C., Sanders D. B., Mazzarella J. M., Soifer B. T., 1995, ApJS, 98, 171
Veilleux S., Sanders D. B., Kim D.-C., 1997, ApJ, 484, 92
Wang J., Hammer F., Athanassoula E., Puech M., Yang Y., Flores H., 2012, A&A, 538, A121
Wright G. S., James P. A., Joseph R. D., McLean I. S., 1990, Nat, 344, 417
Younger J. D., Cox T. J., Seth A. C., Hernquist L., 2007, ApJ, 670, 269

APPENDIX A: CHARACTERISATION OF THE ELLIPTICAL GALAXY REFERENCE SAMPLE AND THE $\gamma - M_{\rm host}$ DIAGRAM

In Section 5.4, we have chosen the sample of Lauer et al. (2007) as reference sample of early-type galaxies to which we compare the cusp properties of our LIRG sample. The original γ'–M_V diagram published in Lauer et al. (2007) shows a strong bimodality between cusp and core galaxies. Lauer et al. (2007) have derived the cusp slope in two different ways, one by fitting the Nuker law parameter γ as in our study, and the other one by calculating the local logarithmic slope at the *HST* resolution limit, defined in their study as γ'. For *HST* WFPC2 in *F555W*, γ' was measured at 0.05 arcsec from the centre. Since the nuclear slope is monotonically decreasing as the radius is going towards zero, this may be regarded as an upper limit on the true slope. The difference between γ and γ' for our reference sample of elliptical galaxies is shown in Fig. A1. Within our magnitude range we find that 15 per cent of the ellipticals have a difference in $\gamma' - \gamma$ of more than 0.1 with an average $\gamma' - \gamma$ of 0.22. This is only relevant for our study to the extent that it will shift some of the core elliptical galaxies into the transition range between cusps and cores ($0 < \gamma < 0.5$), which reduces the bimodal behaviour in the distribution of cusp and core galaxies as seen in Lauer et al. (2007). However, less than 5 per cent of the elliptical galaxies would end up as cusp rather than core galaxies, and hence we find a similar strong correlation between the slope γ and the host magnitude as demonstrated in Fig. 11.

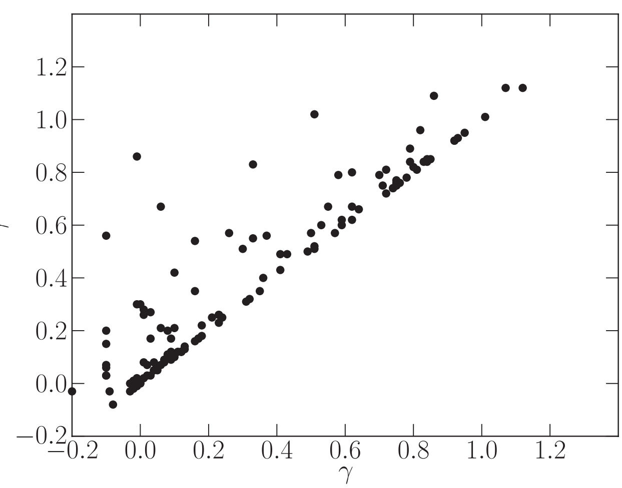

Figure A1. Comparison of the local logarithmic slope at the *HST* resolution limit γ' and the Nuker gamma parameter γ for our reference sample of elliptical galaxies (measurements by Lauer et al. 2007).

APPENDIX B: EXAMPLES OF GALFIT MAPS AND DERIVED RADIAL PROFILES

Here, we present four typical examples of our sample, ranging from strong cusp sources ($\gamma > 1.0$; NGC 6786 north, UGC 9618), to intermediate cusp ($\gamma \sim 0.7$; NGC 3690 east) and core source with a strong unresolved component (NGC 2623) as shown in Figs B1–B3.

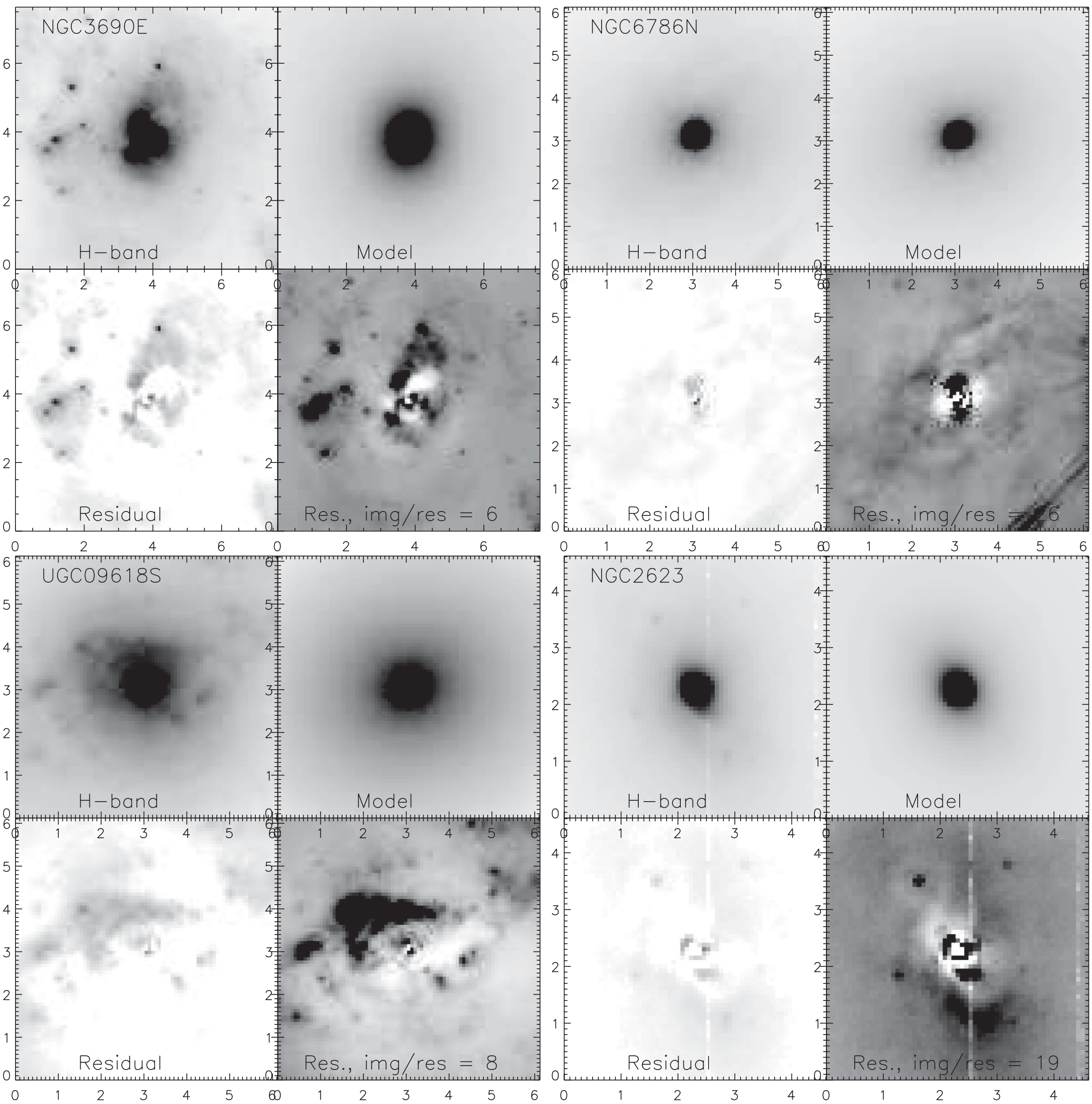

Figure B1. Examples of GALFIT output images for NGC 3690 east, NGC 6786 north, UGC 9618 south and NGC 2623 (scaled with the square root of intensity). In each panel: top left: region of NICMOS image that is fitted. Top right: Galfit model. Bottom left: residual image (shows the difference between model and NICMOS image) with the same brightness level as the NICMOS image. Bottom right: residual image scaled to its maximum brightness (the brightness ratio of NICMOS image to scaled residual map is shown as well at the bottom) to highlight the faint diffuse emission, spiral structure and clusters remaining in the model-subtracted data. The axes are in units of arcsec and the figures are orientated in the observational frame.

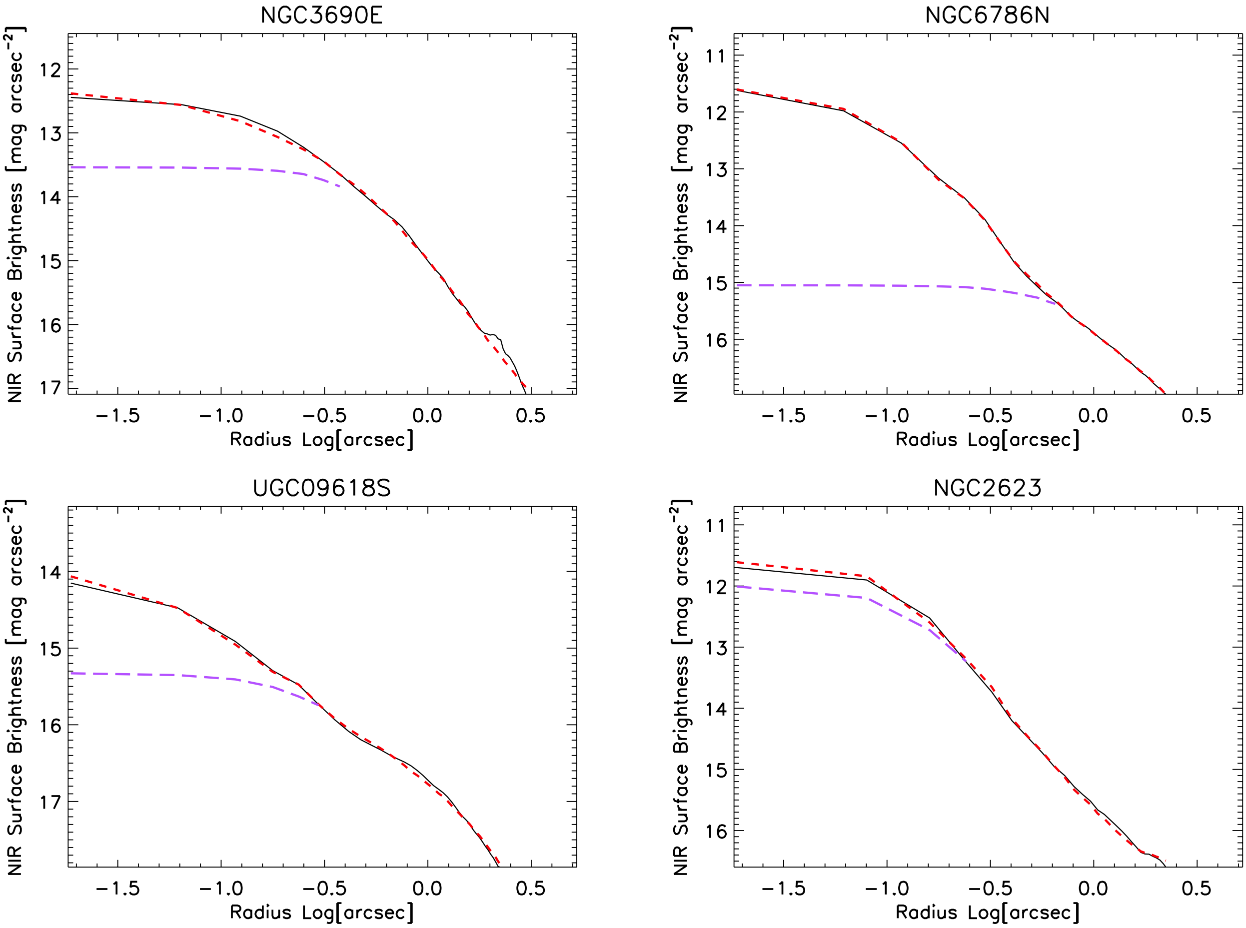

Figure B2. The logarithmic radial profiles of NGC 3690 east (intermediate cusp source), NGC 6786 north (strong cusp source), UGC 9618 south (strong cusp source) and NGC 2623 (core source with PSF). The solid black line is the actual data as observed with *HST* NICMOS at 1.6 μm and the short dashed red line is the radial profile of the GALFIT 2D model. The long dashed blue line shows a fit of the outer envelope with no cusp component, except for the core galaxy NGC 2623 where only the unresolved (PSF) component is excluded.

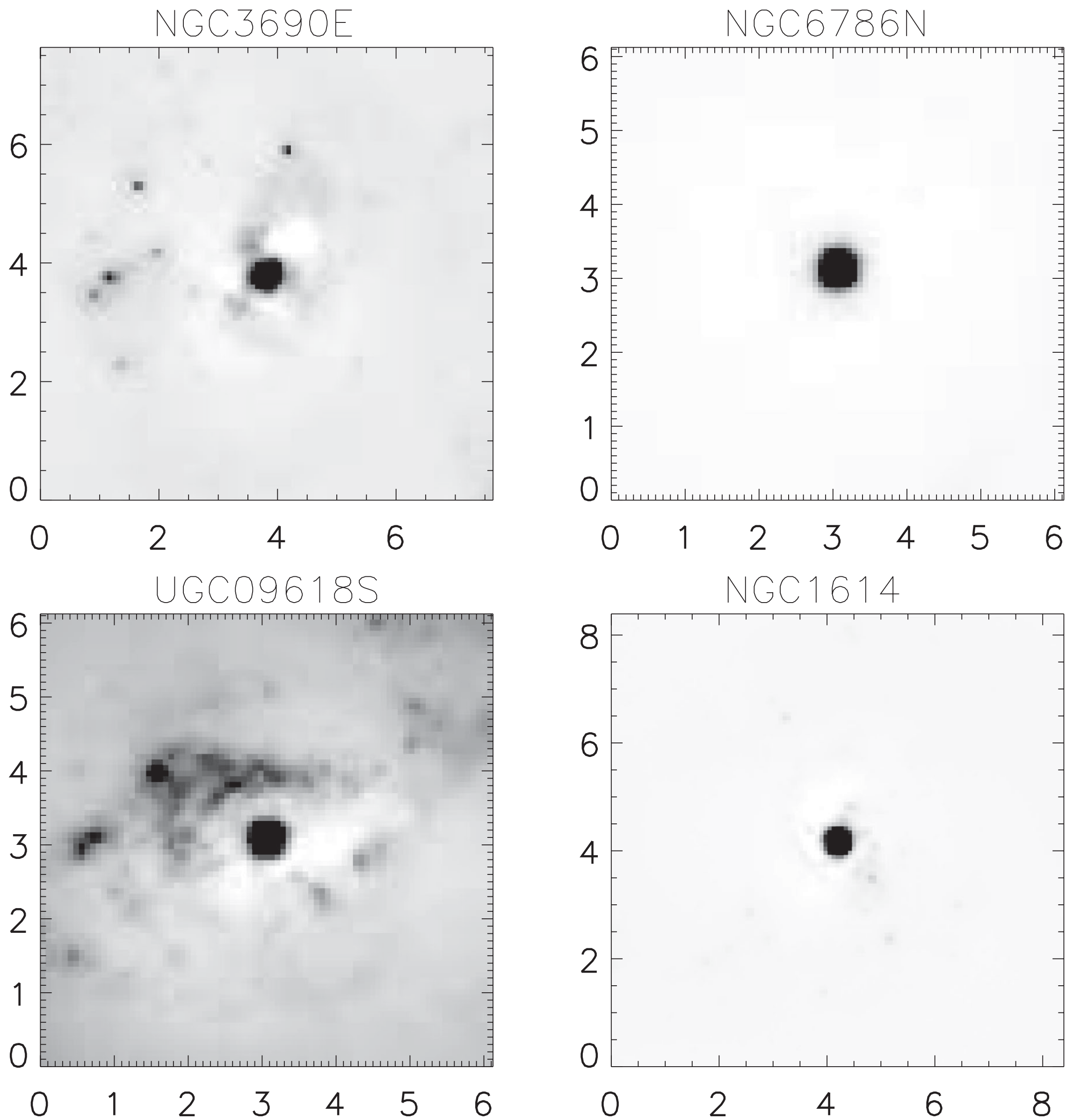

Figure B3. The cusp NIR emission derived from the residual map of the observed data after subtracting the GALFIT model of the outer envelope with no cusp component. The example galaxies are NGC 3690 east, NGC 6786 north, UGC 9618 south and NGC 1614. The axes are in units of arcsec and the figures are orientated in the observational frame. Residual emission that is spatially not associated with the cusp has typically a surface brightness of less than 10 per cent of the cusp surface brightness.

This paper has been typeset from a TEX/LATEX file prepared by the author.